nature communications

Article

https://doi.org/10.1038/s41467-025-56497-3

Degeneracy-breaking and long-lived multimode microwave electromechanical systems enabled by cubic silicon-carbide membrane crystals

Received: 11 January 2024

Accepted: 20 January 2025

Published online: 31 January 2025

Check for updates

Yulong Liu[1,2] ✉, Huanying Sun[1], Qichun Liu[1], Haihua Wu[1], Mika A. Sillanpää[2] & Tiefu Li[3] ✉

Cubic silicon-carbide crystals (3C-SiC), known for their high thermal conductivity and in-plane stress, hold significant promise for the development of high-quality (Q) mechanical oscillators. We reveal degeneracy-breaking phenomena in 3C-phase crystalline silicon-carbide membrane and present high-Q mechanical modes in pairs or clusters. The 3C-SiC material demonstrates excellent microwave compatibility with superconducting circuits. Thus, we can establish a coherent electromechanical interface, enabling precise control over 21 high-Q mechanical modes from a single 3C-SiC square membrane. Benefiting from extremely high mechanical frequency stability, this interface enables tunable light slowing with group delays extending up to an impressive duration of *an hour*. Coherent energy transfer between distinct mechanical modes are also presented. In this work, the studied 3C-SiC membrane crystal with their significant properties of multiple acoustic modes and high-quality factors, provide unique opportunities for the encoding, storage, and transmission of quantum information via bosonic phonon channels.

Silicon-carbide (SiC) is a compound semiconductor that manifests in multiple polytypes, each characterized by distinct crystal structures and stacking sequences of silicon (Si) and carbon (C) atoms. The distinctive advantages offered by individual SiC crystal structures play a pivotal role in tailoring SiC-based devices to specific applications and optimizing their performance[1–3]. The hexagonal structure, such as 4H-SiC and 6H-SiC, represents the most commercially available high-quality SiC crystal form and has garnered widespread attention in the field of quantum information processing due to its potential for hosting quantum bits (qubits)[4–16]. In contrast to hexagonal silicon carbide, cubic silicon carbide (3C-SiC) possesses a zinc-blende crystal structure that closely matches the lattice constant of silicon. Currently, 3C-SiC can be grown directly on a silicon substrate using heteroepitaxy techniques[17]. This compatibility facilitates the integration of 3C-SiC with existing microfabrication and machining technologies on silicon substrates[18–20], which is challenging to achieve with bulk substrates like 4H-SiC and 6H-SiC. In recent years, tensile-loaded thin-film mechanical resonators have achieved significant attention due to their remarkably high Q-factors[21–27]. Crystalline thin films, in general, have a higher theoretical limit for holding tensile stress compared to non-crystalline or amorphous thin membranes[28,29]. The stronger atomic bonding in 3C-SiC contributes to its higher ultimate tensile strength (approaching 18 GPa) compared to hexagonal polytypes[30]. On the other hand, the heteroepitaxial growth techniques can also result in low gradient and high in-plane stress in 3C-SiC thin films[31]. The magnitude of in-plane stress can be controlled by adjusting the growth conditions, including temperature, pressure, and growth rate[32–35]. With these significant advantages, tensile-loaded 3C-SiC is emerging as the material of choice

[1]Beijing Academy of Quantum Information Sciences, Beijing, China. [2]Department of Applied Physics, Aalto University, Aalto, Finland. [3]School of Integrated Circuits and Frontier Science Center for Quantum Information, Tsinghua University, Beijing, China. ✉e-mail: liuyl@baqis.ac.cn; litf@tsinghua.edu.cn

for developing mechanical resonators with high Q-factors[36]. It is important to note that, while 3C-SiC has a high theoretical upper limit of stress, the actual quality factors (Q-factors) of mechanical oscillators made from 3C-SiC are often limited by various factors such as imperfections in the crystal structure[37]. To date, 3C-SiC mechanical microresonator with doubly clamped string[38,39], cantilever[40], trampoline[41], phononic crystal[42], and suspended square membrane[43–45] structures have been developed and measured in the experiment. For the crystalline SiC mechanical resonator, the experimentally achieved highest quality factor reaches around one million (Q-10^6) in high vacuum[39–41].

In the effort to push mechanical oscillators into the quantum realm, the radiation-pressure interaction in laser optomechanical and microwave electromechanical systems plays a crucial role in, e.g., precisely manipulating the macroscopic quantum state of mechanical resonator[46–49], while also providing a transducer interface for connecting phonons with other quantum systems[50–52]. In pursuit of one of the long-standing goals of fundamental tests of quantum mechanics, such as macroscopic-scale Bell tests[53–55], quantum teleportation[56], and tests of quantum gravity[57–59], long-lived mechanical oscillators with extremely low thermal decoherence and pure dephasing rates are highly desired[60]. These urgent needs also arise in the field of quantum information processing, particularly in developing microwave-light interfaces for quantum computation and communication[61–68]. Strain engineering and dissipation dilution with trampoline[69–71], nested[72–75], and acoustic isolation structures[76–80] have been extensively explored in laser and microwave optomechanical devices to mitigate extrinsic mechanical dissipation. While acoustic radiation into the substrate has been significantly suppressed due to weak connecting links to the substrate, this comes at the cost of reduced thermal conductivity to the environment[81–84]. In addition, the carefully designed mechanical structure for dissipative dilution poses significant challenges for the construction of microwave cavity optomechanical devices[28,85–88]. The reduced thermal conductivity, combined with an increase in two-level systems or defects, introduces additional mechanical damping and further diminishes frequency stability[89–92]. These factors present substantial obstacles for engineered high-Q mechanical resonators in achieving lower thermal decoherence and pure dephasing rates in optomechanical devices[93]. Using single-crystal silicon oscillators as an example, phonon bandgap engineering has significantly lowered the energy relaxation rate, achieving an energy quality factor as high as 10^{10}[28]. When these oscillators are combined with optical or microwave resonant cavities, the phonon lifetime remains high at 1.5 seconds. However, temperature-dependent frequency jitter and residual two-level system defects reduce the final coherence time of the vibration mode to the microsecond level, representing a decrease of over four orders of magnitude[77,93]. Therefore, developing mechanical oscillators with both high thermal conductivity and high-quality factors is crucial, as this can enhance frequency stability and increase coherence time. Recently, both theoretical calculations from first principles[94] and experimental measurements at the wafer-scale[95] have revealed that 3C-SiC films exhibit isotropic high thermal conductivity at room temperature, which is the second highest among types of crystals and only surpassed by diamond[96]. In the field of quantum information processing, controlling and dissipating heat generated by quantum devices are crucial for maintaining quantum coherence[97].

In this work, the high thermal conductivity of 3C-SiC mechanical resonators at low temperatures ensures effective thermalization to millikelvin levels, resulting in exceptional frequency stability and extremely small pure dephasing. We highlight the distinctive non-uniform tensile stress found in crystalline membranes and provide insights into the multiple degeneracy-broken mechanical mode pairs and clusters. Furthermore, we explore their potential as numerous high-Q and long-lived phononic modes for quantum information processing, particularly focusing on their extremely low pure dephasing rates and high-frequency stability in conjunction with superconducting quantum circuits. Benefiting from extremely high mechanical frequency stability, this electromechanical interface enables tunable light slowing with group delays extending up to an impressive duration of an hour. While numerous experimental protocols and theoretical studies have aimed to enhance the group delay of light, our work achieves a substantial improvement, offering several orders of magnitude advancement over previous pioneering efforts[78,90,98–104]. We systematically explore on-demand state storage and energy transfer between degeneracy-broken high-Q mechanical modes, achieving quality factors exceeding 10^8. Enabling coherent electromechanical manipulation between long-lived multiple mechanical resonators would be instrumental in advancing the development of phononic memories, repeaters, and transducers for microwave quantum states.

Results

3C-SiC-based microwave electromechanical system

As shown in Fig. 1a, our cavity electromechanical device consists of a three-dimensional (3D) superconducting microwave resonator and a mechanical parallel-plate capacitor chip. The 3D microwave cavity is made from bulk aluminum (Al-6061) with a rectangle recess ($8 \times 12 \times 16$ mm). The panel at the right of the device shows the detailed structure of the mechanical capacitor which is constructed by flipping the metalized 3C-SiC membrane chip on top of another microwave coupling chip with antenna electrodes on its front surface. The SiC membranes are 50 nm thick grown on 400 μm thick, width 5×5 mm square silicon frames (with a low resistivity). The measured X-ray diffraction pattern indicates that the grown SiC thin-film is in 3C phase. The suspended membrane window is a square measuring 500 μm × 500 μm, with the backside silicon of the membrane removed through potassium hydroxide wet etching. The central region of the membrane window was deposited by a 20-nm thick aluminum (Al) film through an electron beam evaporator. The metalized electrode on the suspended 3C-SiC membrane working as the upper plate of the parallel-plate capacitor is circular with a diameter of 200 μm. The lower plate chip is fabricated by sputtering a thin layer of niobium (Nb) with a thickness of 120 nm on top of a high-resistivity silicon substrate (⟨100⟩ oriented) with a thickness of 500 μm.

The zoomed-in subfigure in Fig. 1a, right to the capacitor chip, shows the core area of the mechanical capacitor. The bottom electrode structure, in shape of the letter "H", serves as the lower plate of mechanical parallel-plate capacitor and also functions as a microwave antenna, wireless connecting the mechanical capacitor to the 3D microwave cavity resonator. The center of the membrane is metallized, making the mechanical capacitance changes particularly sensitive to modes with vertical displacement at the membrane's center. Additionally, the presence of a notch in the upper half along the y axis of the bottom electrode facilitates the detection of higher-order vibration modes, particularly those exhibiting vertical displacement at the notch position. This will be discussed in detail in the following sections. An optical microscope photographed the entire parallel-plate electrode area through the SiC membrane window. The green interference pattern indicates the gap between the SiC membrane and the bottom silicon substrate, while the purple interference pattern originates from interference of light inside the vacuum gap of the capacitor. To get a more accurate value, we use a 3D laser microscope to measure the height difference between the top and bottom electrodes. From the line-cut height profile (see Supplementary Note 1), it can be inferred that the vacuum gap is ~576 nm. The side view, cut along the x axis, schematic illustrates the stacked arrangement of the different layers, as presented in Fig. 1b.

The effective lumped-element circuit model of the device is shown in Fig. 1c, where the photon radiation pressure couples the microwave cavity field to the mechanical vibration of the SiC-membrane through a position-dependent capacitor with a

https://doi.org/10.1038/s41467-025-56497-3

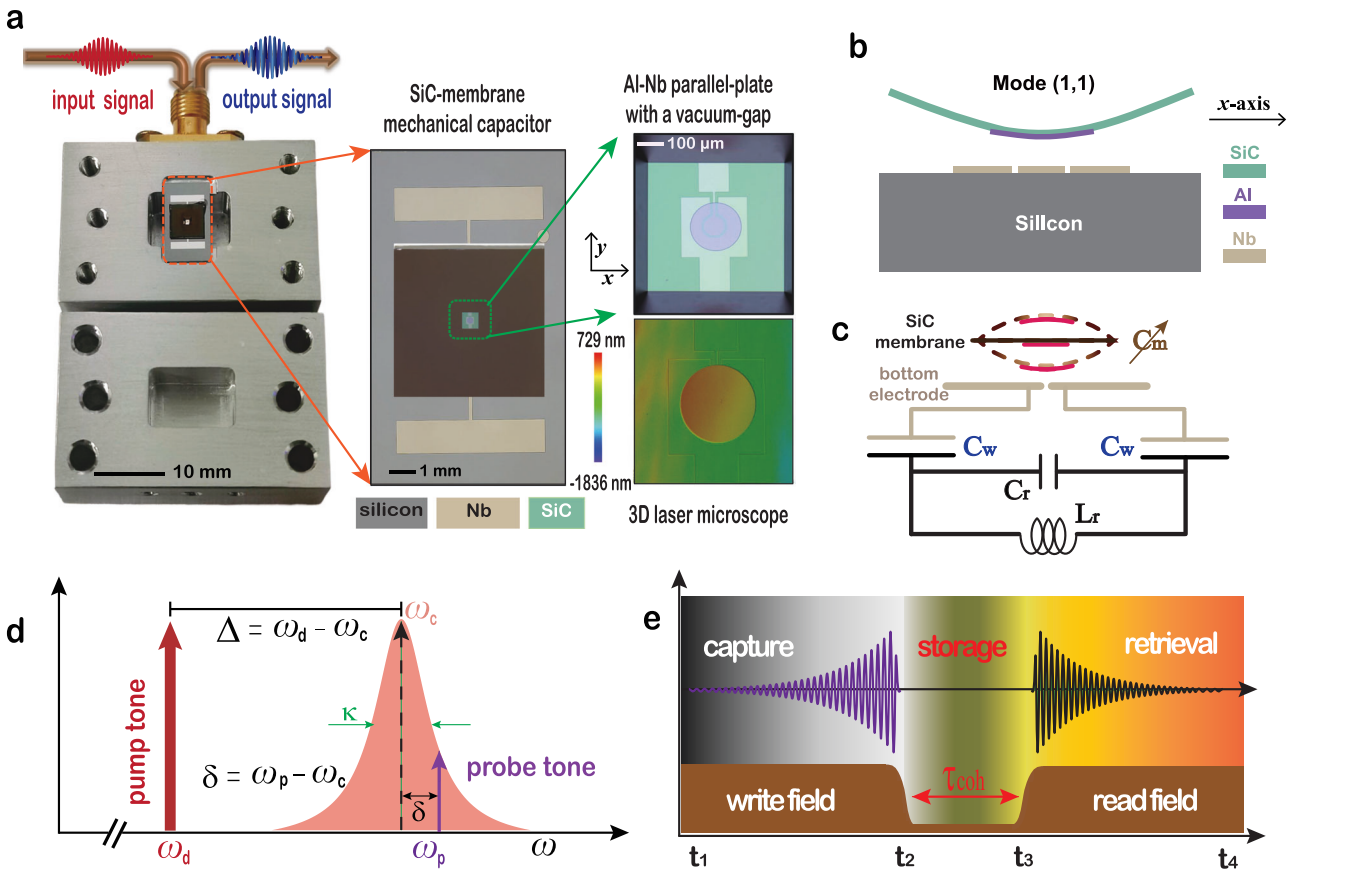

Fig. 1 | The microwave cavity electromechanical interface device and pump-probe schemes used in experiments. a The superconducting 3D-cavity with a SiC-membrane-based mechanical capacitor chip inserted inside its strongest electric field concentration area, forming the dispersive type electromechanical interface device. The zoomed-in area shows the detailed structure of the mechanical parallel-plate capacitor formed by flipping a metalized SiC membrane on top of another bottom electrode microwave antenna. With the geometric center of the bottom electrode as the origin, a notch appears upward in the *y* axis direction. The green arrow marks the core area of the mechanical capacitor, viz., the upper and lower parallel electrode plates and the vacuum interlayer. 3D laser microscope of the parallel-plate electrode region indicates the vacuum gap distance in capacitors. **b** A schematic illustrating the stacked arrangement of the different layers is presented, with a cut along the *x* axis. **c** The effective lumped-element circuit model for our device, where the photon radiation force causes SiC-membrane's mechanical vibration which in turn introduces a tunable capacitor (C_m) and changes the total cavity capacitance. **d** is the continuous wave pump-probe scheme. Strong pump-tone (marked by red arrow) is detuned by ωm from the cavity resonance frequency, and weak probe-tone (marked by purple arrow) is scanning the dynamics of interest that occurred over the cavity mode, which has a linewidth of κ. **e** shows the time sequence of the pulsed pump-probe scheme, which allows an on-demand writing, storage, and reading of microwave pulses by using the long-lived phonons as the core storage element.

capacitance of $C_m(\hat{x})$. The variable mechanical capacitance changes the cavity resonance frequency, forming dispersive type cavity opto-mechanical interaction. The interaction Hamiltonian can be described as $H^i_{int}/\hbar = g_i a^\dagger a \hat{x}_i$. The coupling parameter is $g_i = \partial\omega_c/\partial x_i$, and $\hat{x}_i = x^i_{zpf}(b_i + b_i^\dagger)$ is the displacement operator for each distinct mechanical mode. The mode shape identifier $i = (k, l)$, with k and $l \in \mathbb{N}^+$, refers to the number of humps (antinodes) in the x and y directions of our square 3C-SiC membrane. Here, $a^\dagger$ (a) and $b_i^\dagger$ (b_i) are quantized bosonic creation (annihilation) operators of microwave cavity field and the mechanical mode (k, l), respectively. Here, ω_c is the cavity mode angular resonance frequency, $x^i_{zpf} = \sqrt{\hbar/(2m_i\omega^i_m)}$ is the root-mean-square amplitude of each oscillator's zero-point fluctuations, where m_i and ω^i_m represent the effective mass and the resonance frequency of the corresponding mechanical mode (k, l). When considering photons in the microwave frequency domain, this system is referred to as a cavity electromechanical system. Due to the fact that these mechanical modes are well separated by their resonant frequency, The pump and probe schemes for each mechanical mode will not affect the other. Thus, in the following, we do not specify the identifier 'i' unless it is absolutely necessary.

The Hamiltonian used to describe each mechanical mode that is electromechanically coupled to the microwave cavity field, thereby forming a standard cavity optomechanical system in the microwave regime, is expressed as follows: $H/\hbar = \omega_c a^\dagger a + \omega_m b^\dagger b + g_0 a^\dagger a\left(b + b^\dagger\right)$, where $g_0 = g x_{zpf}$ is the vacuum optomechanical coupling strength. We add a continuous driving tone with frequency Ω_c and amplitude ξ to enhance the effective radiative pressure interaction. As shown in Fig. 1d, the frequency of driving tone is red-detuned to the cavity mode resonant frequency (ω_c) by a mechanical frequency (ω_m), i.e., $\omega_d = \omega_c - \omega_m$. Working in the rotating frame at the pump-tone frequency, the linearized Hamiltonian is described as

$$H/\hbar = \omega_m\left(a^\dagger a + b^\dagger b\right) + G(a^\dagger + a)(b + b^\dagger). \quad (1)$$

Here, $G = g_0\sqrt{N_c}$ is the linearized and driving-field enhanced coupling strength. N_c is the occupation number of photons in cavity mode. Thus, the coupling rate G can be continuously tuned by controlling the power of external coherent driving tone[105].

Taking the cavity and mechanical decay rates into consideration, the set of Heisenberg-Langevin equations of a microwave electro-mechanical device in the presence of a driving tone are given as

follows:

$$\dot{a} = (i\Delta - \kappa/2)a - iG\left(b + b^{\dagger}\right) + \sqrt{\kappa_s}\xi_s, \tag{2}$$

$$\dot{b} = -(i\omega_{\rm m} + \gamma_{\rm m}/2)b - iG(a + a^{\dagger}) + \sqrt{\gamma_{\rm m}}\xi_{\rm m}, \tag{3}$$

where $s = \{\text{in}, \text{ex}\}$. Here, $\kappa_{\rm in}$ and $\kappa_{\rm ex}$ are the intrinsic and external microwave coupling rate to their dissipative bath, κ is the total microwave loss rate. The symbol $\gamma_{\rm m}$ represents the total decay rate of the studied mechanical mode of the square 3C-SiC membrane. The variable Δ denotes the frequency detuning between the driving pump tone and the resonant frequency of the cavity mode, defined as $\Delta = \omega_{\rm d} - \omega_{\rm c}$. The corresponding input noise operators satisfy the commutation relations $\langle \xi_{\rm in}^{\dagger}(t)\xi_{\rm in}(0)\rangle = N_c^{\rm th}\delta(t)$, $\langle \xi_{\rm in}(t)\xi_{\rm in}^{\dagger}(0)\rangle = (N_c^{\rm th}+1)\delta(t)$, and $\langle \xi_o^{\dagger}(t)\xi_o(0)\rangle = N_o^{\rm th}\delta(t)$, $\langle \xi_o(t)\xi_o^{\dagger}(0)\rangle = (N_o^{\rm th}+1)\delta(t)$. $N_c^{\rm th}$ is the cavity mode thermal bath occupation. Subscripts $o = \{\text{ex}, \text{m}\}$ represent the entering noise from cavity mode external pump phase noise $N_{\rm ex}^{\rm th}$, and mechanical thermal bath occupation $N_{\rm m}^{\rm th}$, respectively. From the input-output theory, the output field can be expressed as $a_{\rm out} = \xi_{\rm ex} - \sqrt{\kappa_{\rm ex}}a$. Based on the Wiener-Khinchin theorem, we can now calculate the symmetrized noise power spectrum density (PSD) of the output microwave field[106]. Taking the Fourier transformation of the time derivative equations of Eqs. (2)–(3), and using the commutation relations of noise operators in the frequency domain, the PSD of output mode $S[\omega]$ can be expressed as

$$S[\omega] = \frac{1}{2}\left\langle a_{\rm out}^{\dagger}[-\omega]a_{\rm out}[\omega] + a_{\rm out}[-\omega]a_{\rm out}^{\dagger}[\omega]\right\rangle. \tag{4}$$

The optical-damping rate induced by the microwave drive dynamical backaction is $\gamma_{\rm opt} = 4G^2/\kappa$. In our experiment, the device always works in the weak optomechanical coupling regime ($G \ll \kappa$). When applying the maximum sideband pump power, the optomechanical damping rate will not exceed one percent of the microwave cavity linewidth (viz., $\gamma_{\rm opt} \ll \kappa$). Under the aforementioned conditions, the PSD of the output cavity field is ultimately expressed as[107]

$$S[\omega] = n_{\rm add} + \frac{4\kappa_{\rm ex}\kappa N_c^{\rm th}}{\kappa^2 + 4\tilde{\delta}^2} + \frac{4\eta\gamma_{\rm opt}\gamma_{\rm tot}\left(N_{\rm m}^{\rm th} - 2N_c^{\rm th}\right)}{\gamma_{\rm tot}^2 + 4\tilde{\delta}^2}, \tag{5}$$

where $\tilde{\delta} = \omega - \omega_m$, and $\eta = \kappa_{\rm ex}/\kappa$. The total mechanical damping rate is defined as $\gamma_{\rm tot} = \gamma_{\rm m} + \gamma_{\rm opt}$.

During the microwave measurement, the added noise, $n_{\rm add}$, mostly coming from the HEMT amplifiers and to a small extent from vacuum noise, creates the background noise floor of the measured PSD. The effective microwave thermal occupation $N_c^{\rm th}$ may come from the thermal effects caused by defects in bulk superconducting cavities. These defects or impurities can induce thermal effects through ways of increasing surface resistance, causing localized heating, or promoting quasiparticle generations. $N_{\rm m}^{\rm th}$ is the effective thermal occupation of mechanical mode and transfers into the microwave output field via the electromechanical coupling. The second term in Eq. (5) indicates that cavity thermal noise spectrum is a Lorentzian type with a linewidth of κ. The last term in Eq. (5) indicates that the damped mechanical mode is featured as a Lorentzian spectrum with a total linewidth of $\gamma_{\rm tot}$. The full-noise PSD contains two Lorentzian peaks, where the mechanical sidebands are superimposed on the Lorentzian peak of the cavity thermal emission.

When measuring the PSD spectrum, we select a driving power that allows the optomechanical damping and cavity thermal occupation to be negligible, i.e., $\gamma_{\rm opt} \ll \gamma_{\rm m}$, and $N_c^{\rm th} \simeq 0$. Under such conditions, the expression of the PSD spectrum reduces into a standard Lorentzian function

$$\tilde{S}[\omega] = n_{\rm add} + \mathcal{G}\frac{\gamma_{\rm m}/2}{(\gamma_{\rm m}/2)^2 + (\omega - \omega_{\rm m})^2}, \tag{6}$$

where $\mathcal{G} = 2\eta\gamma_{\rm opt}N_{\rm m}^{\rm th}$.

In the following sections, we will first employ the power spectral density (PSD) method to identify all the mechanical modes detectable by the microwave cavity. We will particularly focus on how the breaking of degeneracy generates multiple detectable high-Q mode pairs in the square 3C-SiC membrane. Additionally, we will conduct ringdown measurements for each distinct mechanical mode. The PSD provides the total decay rate, while the ringdown measurements yield the energy decay rate. By comparing the decay rates obtained from these two measurement techniques, we will demonstrate the exceptional performance of the square 3C-SiC membrane as a high-Q mechanical resonator, particularly emphasizing its extremely low pure dephasing at low temperatures.

To leverage its outstanding frequency stability, we will employ a continuous pump-probe scheme, as shown in Fig. 1d, to demonstrate a new record in the passive storage of classical microwave signals. Furthermore, the pulsed pump-probe sequences depicted in Fig. 1e will enable on-demand ground-state cooling, writing, storage, and reading of microwave coherent states based on the long-lived phononic modes of the 3C-SiC membrane. Finally, we will also demonstrate coherent energy transfer between distinct mechanical modes.

Degeneracy-breaking and multiple high-Q mechanical mode-pairs of a square 3C-SiC membrane

The device is mounted on a suspended oxygen-free copper plate, which is connected to the mixing chamber of a dry dilution refrigerator (with a minimum operating temperature of 8.9 mK) via copper braids. Without a mechanical isolation system, the mechanical modes cannot be thermalized below 500 mK. We provide a detailed discussion of the mechanical isolation techniques in Supplementary Note 2. The sheet resistance of the grown 3C-SiC, measured at room temperature, is ~1 Ω · cm. It is essential to verify the compatibility of this low-resistance 3C-SiC semiconductor material with microwave radio frequency circuits, particularly regarding whether this material will introduce significant dissipation to the superconducting cavity mode. As shown in Fig. 1c, the probe field can be used to detect the cavity responses under different external pump powers. In the low pump power regime (e.g., $P = -30$ dBm), the measured intrinsic and external decay rates are $\kappa_{\rm in}/2\pi = 80$ kHz and $\kappa_{\rm ex}/2\pi = 120.25$ kHz, respectively. Under strong pump power (e.g., $P = 20$ dBm), the cavity total linewidth decreases to $\kappa/2\pi = 160$ kHz. The frequency of the resonant cavity is quite stable. As the number of photons in the cavity increases, the resonant frequency changes only ~3 kHz. The cavity S_{21} measurements indicate that our 3C-SiC membrane is well-compatible with superconducting resonators for microwave applications.

We now read out these mechanical modes through electromechanical interactions by applying a weak continuous microwave pump tone to the cavity field via the SMA-type (depicted in Fig. 1a) input port of the 3D microwave resonator. The driving frequency is red-detuned to the cavity resonance by each mechanical resonance frequency, i.e., $\Delta = -\omega_{\rm m}^i$. The beam-splitter-like interaction terms $H_{\rm int}^i/\hbar = G_i(a^{\dagger}b_i + b_i^{\dagger}a)$ indicate that the voltage signal of the output microwave field contains information such as the mechanical resonance frequency and cavity field dressed mechanical linewidth.

Figure 2a shows the measured PSD of the output microwave field in a wide frequency range (up to 2.37 MHz). For this device, 21 mechanical modes coupled to the cavity field have been measured. The Q-factors for each mechanical mode are measured through

https://doi.org/10.1038/s41467-025-56497-3

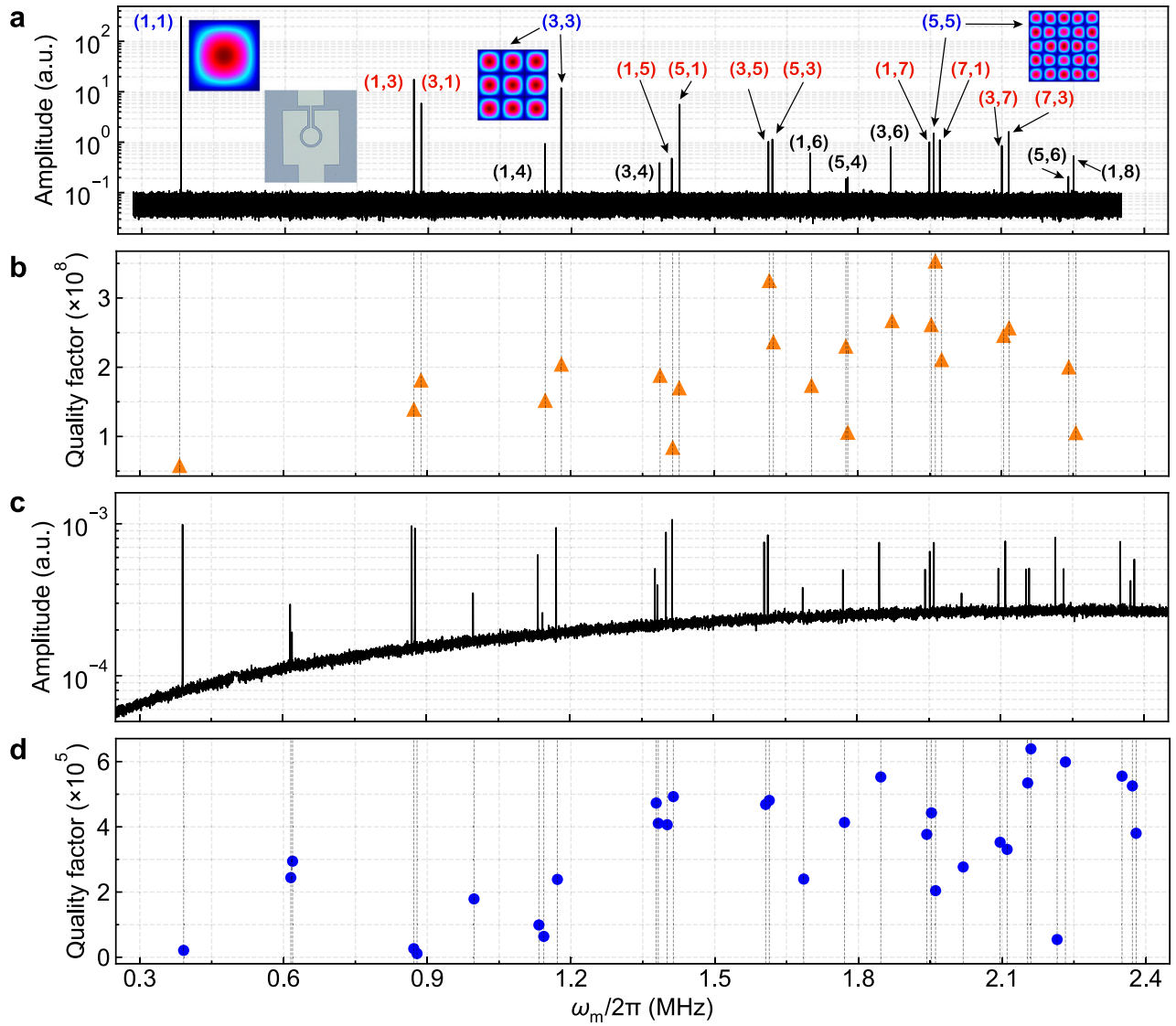

Fig. 2 | The microwave and optical readout of multiple mechanical modes from a single square 3C-SiC crystalline membrane. a The microwave power spectral density (PSD) readout of mechanical modes and the corresponding mode numbers (k, l) are labeled around each peak of the measured mechanical modes. The finite element method (FEM) simulations with non-uniform tensile stress for modes (1,1), (3,3), and (5,5) are presented. A notch structure extends upward along the y axis of the bottom electrode. **b** The corresponding Q-factors for each mechanical mode in a dilution refrigerator. The Q-factors are obtained through the stroboscopic ringdown measurements. Twenty-first mechanical modes can be measured based on their independent optomechanical interaction with the same cavity field. **c** The mechanical modes from the same crystalline 3C-SiC square membrane are detected with a laser Doppler vibrometer at room temperature and corresponding Q-factors are present in **d**. The laser spot is focused near the center of the square membrane.

stroboscopic ringdown technology (see Supplementary Note 3) and are presented in Fig. 2b. Remarkably, 19 of the 21 detected mechanical modes have quality factors exceeding 10^8.

As shown in Fig. 1b, c, our studied electromechanical device is particularly sensitive to those mechanical modes that exhibit a central vertical displacement. For a square membrane, when the mode numbers k and j are equal, and both are odd, the mode shapes of these special modes consistently display a central vertical displacement, making them relatively easier to read out electromechanically. The finite element method (FEM) solutions in COMSOL for the mode shapes of the detected modes, such as (1,1), (3,3), and (5,5), are presented around each measured mode peak in Fig. 2a. The fundamental drumhead (1,1) mode has a resonant frequency of $\omega_m^{(1,1)}/2\pi$=382.15 kHz and a Q factor of $Q^{(1,1)} = 5.76 \times 10^7$. The modes (3,3) and (5,5) have frequencies and Q-factors of $\omega_m^{(3,3)}/2\pi = 1.17$ MHz with $Q^{(3,3)} = 2 \times 10^8$, and $\omega_m^{(5,5)}/2\pi = 1.96$ MHz with $Q^{(5,5)} = 3.5 \times 10^8$, respectively.

The fundamental mode is followed by a pair of nearly resonant mechanical modes with mode numbers (1,3) and (3,1), having quality factors of 1.4×10^8 and 1.8×10^8, respectively. Additionally, we identify another set of four nearly resonant mode pairs with higher mode numbers: (1,5) and (5,1), (3,5) and (5,3), (1,7) and (7,1), as well as (3,7) and (7,3). Other detected mechanical modes of the square 3C-SiC membrane include (1,4), (3,4), (1,6), (5,4), (3,6), (5,6), and (1,8). In conclusion, these electromechanically readable distinct modes or mode pairs share a common characteristic: the mode number k must be an odd number.

Next, we focus on the physical mechanism of electromechanical reading of the near-resonant mode pairs in this square 3C-SiC membrane, specifically the pairs (k, l) and (l, k) as demonstrated in Fig. 2a, where both k and l are unequal odd numbers. Considering a square membrane with uniform biaxial tensile stress, e.g., widely studied amorphous silicon-nitride (SiN)[27,108–112], the natural vibration frequencies of a square film in the stress-governed regime (membrane) in

https://doi.org/10.1038/s41467-025-56497-3

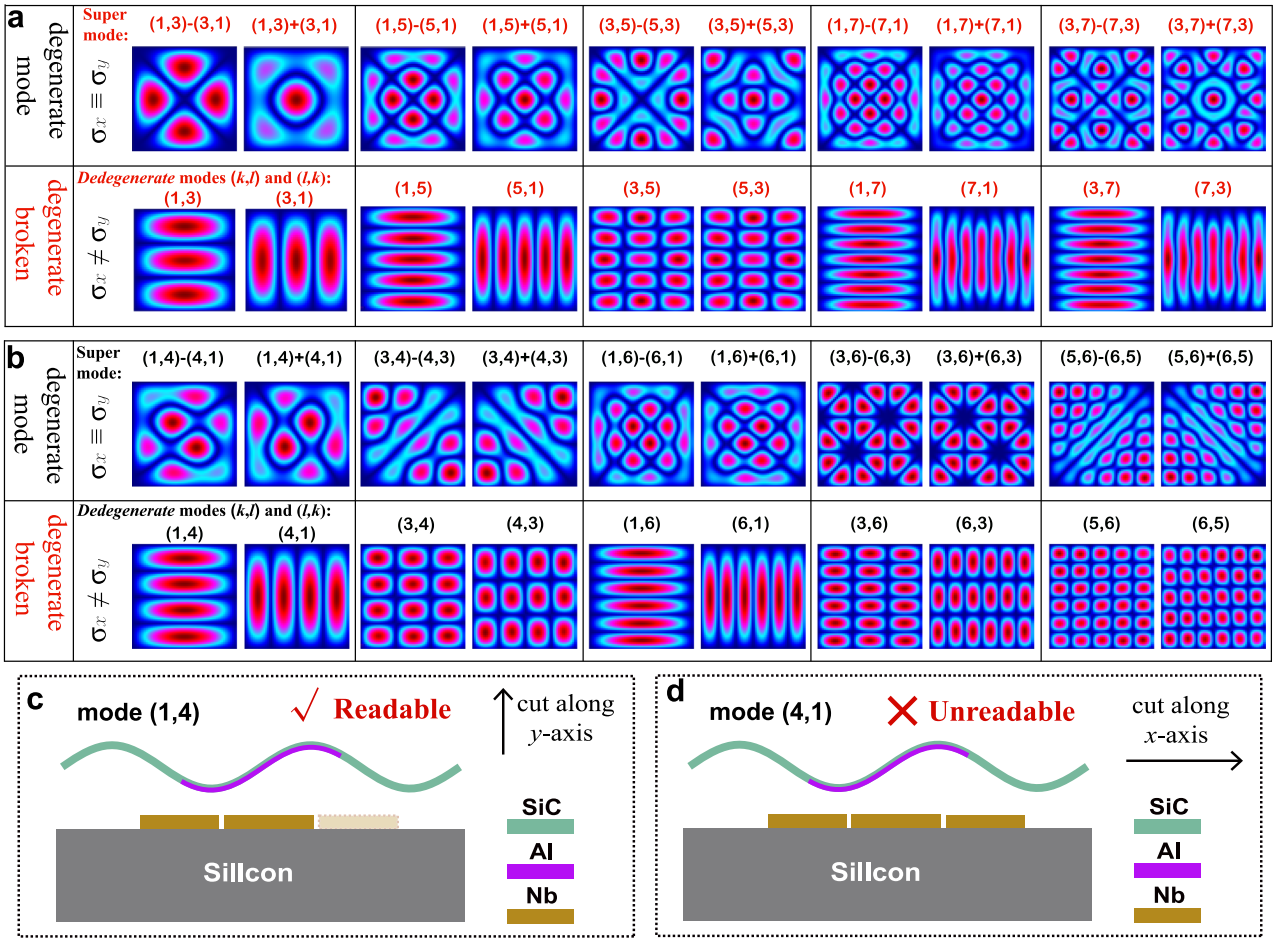

Fig. 3 | The mode shapes and effective mechanical capacitance for a square membrane in the stress-governed regime. The first (second) row in **a** shows the (k, l) mode shapes with uniform (non-uniform) biaxial tensile stress $\sigma_x \equiv \sigma_y$ ($\sigma_x \neq \sigma_y$). The mode numbers k and l presented in **a** are both odd numbers. **b** presents the mode shapes for mechanical (k, l) modes with odd mode number k and even number l. Similarly to **a**, the first and second rows correspond to uniform and non-uniform biaxial tensile stress cases, respectively. For odd k and even l, **c**, **d** schematically illustrate how the vertical mechanical oscillations of the degenerate-broken (k, l) and (l, k) modes induce changes in the corresponding mechanical capacitance, using $k = 1$ and $l = 4$ as an example.

vacuum are given by

$$\omega_{\mathrm{m}}^{(k,l)}/2\pi = \frac{1}{2L}\sqrt{\frac{\sigma}{\rho}(k^2+l^2)}, \tag{7}$$

with the result that $\omega_{\mathrm{m}}^{(k,l)} = \omega_{\mathrm{m}}^{(l,k)}$. Here, σ is the biaxial tensile stress and ρ is the density of the material. Equation (7) indicates that when $k \neq l$, the modes (k, l) and (l, k) exhibit two different mode shapes, $\Psi_{(k,\,l)}$ and $\Psi_{(l,\,k)}$, but have exactly the same frequency, which is referred to as degenerate modes. Since the frequencies are indistinguishable, if the square membrane is excited at this frequency, both of these degenerate modes will oscillate simultaneously. The overall vibration response of the square membrane will be a combination of all the degenerate mode shapes, represented as supermodes: $\Psi_{kl}^{\pm} = a\Psi_{(k,l)} \pm b\Psi_{(l,k)}$, where $a^2 + b^2 = 1$. Clearly, the formed supermodes share the same frequency as the original degenerate modes and remain degenerate.

The FEM simulations for the supermodes $\Psi_{kl}^{\pm}$ are illustrated in the first row of Fig. 3a. Additionally, the mode shapes of the original degenerate modes $\Psi_{(k,\,l)}$ and $\Psi_{(l,\,k)}$ resemble the patterns shown in the second row of Fig. 3a. When the modes (k, l) and (l, k) are degenerate, their mode shapes will be symmetric, rotated by 90°. Interestingly, both these mode shapes feature a central vertical up-and-down vibrational displacement. The superposition of mode shapes $\Psi_{(k,\,l)}$ and $\Psi_{(l,\,k)}$ can result in two situations: constructive interference $[\Psi_{kl}^{+} = (\Psi_{(k,l)} + \Psi_{(l,k)})/\sqrt{2}]$ and destructive interference $[\Psi_{kl}^{-} = (\Psi_{(k,l)} - \Psi_{(l,k)})/\sqrt{2}]$ of the vibration displacements. Constructive interference results in an enhancement of the central vertical displacement, whereas destructive interference leads to a reduction, ultimately eliminating the central vertical displacement. In conclusion, for unequal odd k and l, only the constructive superposition Ψ_{kl}^{+} retains a central vertical displacement, which can modulate the mechanical capacitance and be read out through microwave cavity electromechanical interaction in this work. It is important to emphasize that the above conclusion applies specifically under the condition of uniform tensile stress on a square membrane, where $\sigma_x = \sigma_y$.

However, a significant difference between the above theoretical analysis and our experiment is that, we detect near-resonance mode-pairs (indicated by red-colored mode numbers in Fig. 2a) instead of a single super mode Ψ_{kl}^{+} resulting from constructive superposition. For a square membrane resonator, when the tensile stress becomes non-uniform (i.e., $\sigma_x \neq \sigma_y$), the supermodes $\Psi_{kl}^{\pm}$ will be broken and reduce to near-resonance (k, l) and (l, k) mode-pairs with distinct mode shapes $\Psi_{(k,\,l)}$ and $\Psi_{(l,\,k)}$, respectively. In later sections, this phenomenon is referred to as "*dedegenerate*". The second row of Fig. 3a shows the FEM simulations of the mode shapes for the dedegenerate (k, l) and (l, k) mode pairs with $\sigma_x \neq \sigma_y$. Remarkably, both dedegenerate mode pairs

are characterized by central vertical displacement, which can induce changes in mechanical capacitance. Thus, the degeneracy-breaking process allows the cavity to electromechanically read out both mechanical modes within the near-resonance mode pair. This represents a significant difference compared to a membrane with uniform biaxial stress, where only the constructive supermodes can be electromechanically read out.

It is worth noting that even if the stress distribution of a thin membrane, such as a well-studied SiN membrane[113–116], is uniform at room temperature, stress redistribution, and non-uniformity may occur during the cooling process of the refrigerator due to chip deformation. However, the stress distortion caused by this deformation often significantly reduces the quality factor of the mechanical modes. In our experiment, all detected mode pairs exhibit high-Q behavior, with a quality factor Q exceeding 10^8. To further rule out this possibility, Fig. 2c and d display the measured mechanical resonance and the corresponding Q-factors at room temperature, obtained using a laser Doppler vibrometer with the laser spot focused near the center of the square membrane. The measurement setup and laser PSD result of each detected mechanical mode are presented in Supplementary Note 4. Due to the fact that the laser spot cannot be exactly located at the center of the square membrane, the method using a Doppler vibrometer can detect more mechanical modes than the method using microwave cavity optomechanical interaction. We can still observe near-resonance mechanical modes at room temperature that correspond to the results detected at 10 mK, as presented in Fig. 2a, b. It is evident that the mechanical modes (k, l) and (l, k) are originally non-degenerate, and that the 3C-SiC membrane initially exhibits non-uniform biaxial tensile stress from room temperature. Additionally, Fig. 2 illustrates that the Q values of all mechanical modes improve by three orders of magnitude as the environmental temperature decreases from room temperature to ~10 mK.

The biaxial tensile stresses used in the COMSOL simulation shown in Fig. 3 are $\sigma_x = 242$ MPa, and $\sigma_y = 240$ MPa, respectively. The simulated frequencies show good agreement with the frequencies measured by the laser Doppler vibrometer. The finite element analysis also indicates that the dedegenerate initiates when difference in biaxial tensile stresses exceeds 0.1 Mpa. Once the stress difference reaches 1 Mpa, the dedegenerate mechanical modes (k, l) and (l, k) exhibits completely distinct mode shapes. In the special case where the odd mode number k equals l, it is evident that, despite the biaxial tensile stress not being uniform, only a single mode exists, with no degenerate modes.

As discussed in previous sections, the central area of 3C-SiC square membrane is metallized (as shown in Fig. 1a), making the change in mechanical capacitance particularly sensitive to mechanical modes with central drumhead shapes. However, we emphasize that the notch structure along the y axis in the bottom electrode (see inset of Fig. 2a for the detail) of the mechanical capacitor enables the detection of higher-order mechanical modes, particularly those exhibiting significant vertical displacement around the notch area. We thus move to demonstrate how the degenerance-breaking affect the cavity electromechanical readout of the mechanical modes with one of the mode number k or l is even and the other is odd. In Fig. 3b, the first row illustrates the mode shapes under uniform tensile stresses, where the mode shape of degenerate superposition generated supermodes $\Psi_{kl}^{\pm}$ exhibit a 90° rotational symmetry. Notably, although the bottom antenna electrode contains a notch structure, the simultaneous presence of peaks and dips around the central metallized region of the square 3C-SiC membrane cancels each other out, resulting in nearly unchanged mechanical capacitances. Therefore, when one of the mode numbers k or l is even, and the other is odd, all these degenerate supermodes cannot be read out electromechanically through the cavity field.

Remarkably, the breaking of rotational symmetry combining with the asymmetric notch design of the capacitor bottom electrode, enables the selective readout from mechanical modes (k, l) and (l, k). As shown in Fig. 2a, dedegenerate modes include (1,4), (3,4), (1,6), (5,4), (3,6), (5,6), and (1,8) are read out with Q-factors over 10^8. For odd k and even l, the FEM simulation and the mode shapes for mode pair (k, l) and (l, k) under non-uniform biaxial tensile stress are shown in the second row of Fig. 3b. Owing to the notch that extends upward along the y axis of the bottom electrode, only the (k, l) modes from the dedegenerate mode pair, defined by odd k and even l mode number, exhibit significant variations in mechanical capacitance, thereby facilitating their detection by the microwave cavity. Here the positive integer l should be greater than 2 because, for the (1,2) mode, the area with the largest amplitude is not covered by the metallized aluminum electrode. In contrast, the (l, k) modes do not induce significant capacitance changes and, therefore cannot be detected.

Using $k = 1$ and $l = 4$ as an example, for mode (1,4), the standing wave nodes are distributed along the y direction, which is why the schematic diagram in Fig. 3c employs a cross-sectional view along the y axis. The mode vertical displacement combing the bottom antenna notch introduces the mechanical capacitance changes. In contrast, for the (4, 1) mode, the standing wave nodes are distributed along the x direction, necessitating a cross-sectional view along the x axis in the schematic diagram as shown in Fig. 3d. However, the capacitance changes resulting from the vertical displacement cancel each other out, rendering the (4, 1) mode undetectable by the microwave cavity. In the final scenario, when both mode numbers are even, despite the occurrence of degeneracy breaking, the detectability of these modes is constrained by negligible capacitance changes, rendering them undetectable.

Multiple degeneracy-broken mechanical modes with extremely low pure dephasing

The strength of optomechanical interactions in a microwave cavity electromechanical system can be quantified by the vacuum coupling rate g_0. For the detected 21 mechanical modes, the vacuum coupling rate for each mode is presented in Fig. 4a. Finite element modeling and a comparison between the simulation of g_0 and the measurement results are presented in Supplementary Note 5.

Although the fundamental (1,1) mode exhibits the strongest g_0, its Q factor is only 5.7×10^7, which is the minimum among all the detected modes. Considering both the mechanical Q value and the resolved-sideband condition, our subsequent studies will focus on the mechanical mode (1,3) highlighted in red in Fig. 4a. Meanwhile, the inset in Fig. 4a shows how the vertical displacement of mode (1,3) changes the mechanical vacuum-gap capacitance, with a cut along the y axis. This mode has a resonance frequency of $\omega_m/2\pi = 871.318$ kHz and a remarkable Q factor of 1.18×10^8.

Using Eq. (6) to fit the measured PSD yields the mechanical decay rate for each mechanical mode. As an example, Fig. 4b shows the measured PSD spectrum of mechanical mode (1,3), and the fitted energy decay rate is $\gamma_m/2\pi = 8.2$ mHz. Simultaneously applying driving and probe tone with a frequency difference by ω_m can effectively excite the mechanical motion. After the driving tone is abruptly turned off, the ringdown trace of the fundamental drumhead mode is shown in Fig. 4c. Using exponential fitting, we obtain the energy decay of the mechanical resonator with a rate of $\gamma_m/2\pi = 8.13$ mHz, which agrees well with the value obtained from the PSD measurement in Fig. 4b. In addition to the energy decay rate and lifetime, pure dephasing rate is also an important parameter to be considered.

Although the energy spectrum tests and the time domain ringdown tests suggest that pure dephasing has a very small effect, we will record the ringdown data for an extended duration using I/Q

https://doi.org/10.1038/s41467-025-56497-3

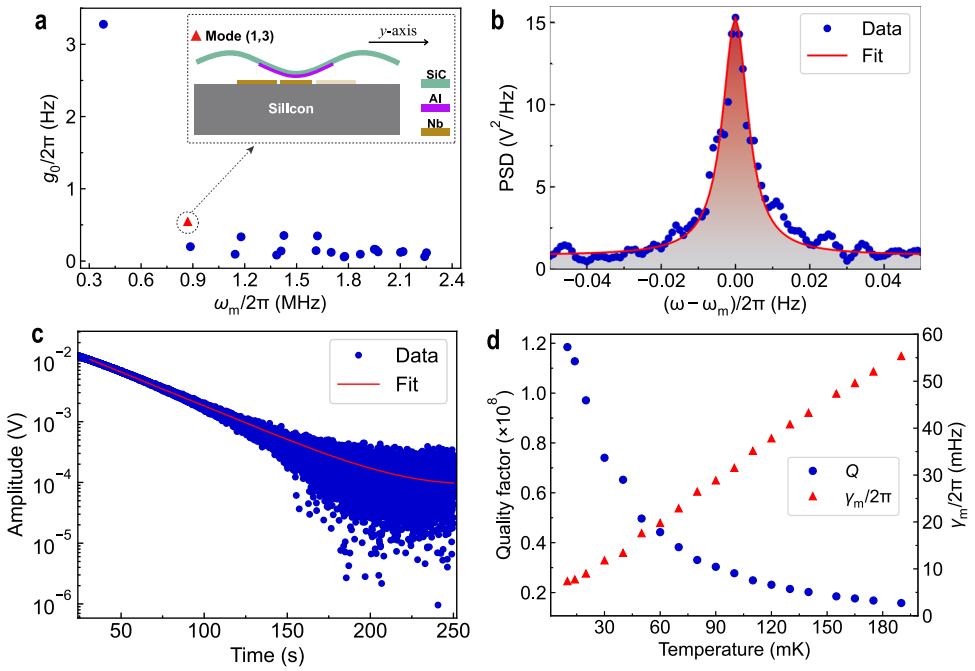

Fig. 4 | Electromechanical coupling strengths and *Q* values as a function of refrigerator temperature sweep. a The single-photon coupling strength between each mechanical mode to the common microwave cavity field. The inset in **a** illustrates how the vertical displacement of mode (1,3) affects the mechanical vacuum-gap capacitance, with a cut along the *y* axis. **b** The PSD of the mechanical mode (1,3) obtained from the IQ measurement with a 1000 seconds sampling time. **c** The mechanical energy ringdown shows a decay rate of $\gamma_m/2\pi = 8.13$ mHz. The measured mechanical resonant frequency is $\omega_m/2\pi = 875.318$ kHz and the spectrum linewidth via fit is obtained as $\gamma_m/2\pi = 8.2$ mHz, corresponding to a quality factor of $Q = 1.18 \times 10^8$. **d** The linewidth and *Q*-value of the mechanical mode with the strongest coupling to the microwave cavity (marked by blue dot in **a**) evolve with the refrigerator's operating temperature.

sampling[108]. By directly comparing the linewidth of the energy spectrum obtained after FFT transformation with the energy relaxation rate derived from direct fitting (see Supplementary Note 6), we can accurately determine the magnitude of pure dephasing, which is measured at $\gamma_\varphi = 0.28$ mHz. These results indicate that dephasing does not significantly contribute to decoherence in the SiC square membrane resonators.

Recalling the measurements made by the Doppler vibrometer at room temperature, the *Q* factor for mode (1,3) was only 2.6×10^4. This performance underwent an impressive improvement of almost four orders of magnitude when operating at a low temperature of ~10 mK. To investigate how the decrease in temperature affects the evolution of the *Q*-factors, a temperature sweep experiment was conducted. The measured *Q*-factors of mode (1,3) as a function of the dilution refrigerator operating temperature are depicted in Fig. 4d. The linewidth (*Q* factor) of the mechanical oscillator continues to decrease (increases) as the operating temperature decreases, showing a linear dependence. For every 10 mK increase in temperature, the linewidth increases by 2.66 mHz. Furthermore, the frequency of the mechanical oscillator remains highly stable across the tested temperature range of 10 mK to 190 mK, exhibiting a variation of less than 1 mHz over a duration of one day.

For instance, the focused study on the mechanical mode (1, 3) of the 3C-SiC square membrane reveals an energy decay time of of ~$T_1 = 19.9$ seconds, a total linewidth of $\gamma_m/2\pi = 8.2$ mHz, particularly with an extremely low pure dephasing rate of of $\gamma_\varphi = 0.28$ mHz. Table 1 summarizes the pure dephasing of all detected mechanical modes and their proportion in the total linewidth. These initial characterizations enable us to conclude that the degeneracy-breaking 3C-SiC membrane supports multiple mechanical modes with exceptional performance, particularly characterized by extremely low pure dephasing. Motivated by this enhanced mechanical frequency stability, we proceed to demonstrate its potential application as a classical microwave memory device.

Hour-level group-delay and slow-light with extremely stable mechanical modes

The pure dephasing of the studied 3C-SiC square membrane is measured at only 0.28 millihertz, constituting just 3.5% of the total linewidth. In comparison, the pure dephasing value for silicon-nitride (SiN), which has made significant advancements in improving quality factors, accounts for over 25% of the total linewidth[21,22,90,92,108]. This results in at least an 86% reduction in frequency instability for the 3C-SiC resonator compared to SiN resonators. Consequently, our 3C-SiC resonator exhibits remarkable frequency stability, as demonstrated by a frequency shift of >1 millihertz per day. The narrow linewidth of SiN mechanical resonators has resulted in a reported maximum group delay on the order of hundreds of seconds[117]. In this context, the limitation for high-*Q* mechanical resonators is often frequency instability. In the following section, we will demonstrate how the significantly improved frequency stability of the focused 3C-SiC square membrane in this work can contribute to setting a new record in the passive storage of propagating microwave signals.

We now demonstrate the transmission response of a weak probe-tone with frequency ω_p and amplitude ε, also well known as the continuous field pump-probe experiment. The scheme has been depicted in Fig. 1d, where the pump-tone is red-detuned to cavity resonance frequency by $\Delta = -\omega_m$. The weak probe tone is scanned by continuously changing frequency, and the dynamics of interest occur when the probe frequency enters the microwave cavity resonance regime. Working in the rotating frame at the pump-tone frequency ω_d, and considering the input-output relations, the transmission coefficient is given as

$$t = 1 + \frac{\eta\kappa(i\delta - \gamma_m/2)}{(i\delta - \gamma_m/2)(i\delta - \kappa/2) + G^2}. \tag{8}$$

The amplitude and phase responses can be calculated with the relations $T = |t|^2$, and $\varphi = \arg(t)$, respectively. The group delay (slow-light

Table 1 | The pure dephasing and its proportion of the total linewidth for each mechanical mode

Mode number	Frequency ($2\pi\cdot$)	Total linewidth ($2\pi\cdot$)	Pure dephasing ($2\pi\cdot$)	Proportion
(1,1)	382.147 kHz	6.83 mHz	0.22 mHz	3.22%
(1,3)	871.318 kHz	8.2 mHz	0.28 mHz	3.41%
(3,1)	885.413 kHz	5.31 mHz	0.4 mHz	7.53%
(1,4)	1.144 MHz	7.9 mHz	0.33 mHz	4.17%
(3,3)	1.178 MHz	6.04 mHz	0.25 mHz	4.13%
(3,4)	1.384 MHz	7.55 mHz	0.16 mHz	2.11%
(1,5)	1.41 MHz	17.46 mHz	0.27 mHz	1.54%
(5,1)	1.426 MHz	8.56 mHz	0.28 mHz	3.27%
(3,5)	1.612 MHz	5.26 mHz	0.28 mHz	5.32%
(5,3)	1.621 MHz	7.1 mHz	0.23 mHz	3.23%
(1,6)	1.7 MHz	10.05 mHz	0.22 mHz	2.18%
(5,4)	1.776 MHz	8.09 mHz	0.37 mHz	4.57%
(3,6)	1.868 MHz	7.28 mHz	0.23 mHz	3.15%
(1,7)	1.949 MHz	7.75 mHz	0.26 mHz	3.35%
(5,5)	1.959 MHz	5.88 mHz	0.32 mHz	5.44%
(7,1)	1.971 MHz	9.7 mHz	0.31 mHz	3.19%
(3,7)	2.101 MHz	8.91 mHz	0.31 mHz	3.47%
(7,3)	2.116 MHz	8.38 mHz	0.18 mHz	2.14%
(5,6)	2.24 MHz	11.72 mHz	0.5 mHz	4.26%
(1,8)	2.25 MHz	22.58 mHz	0.62 mHz	2.74%

time τ) is obtained from the slope of phase-response, i.e., $\tau = \partial\varphi/\partial\omega_p = \partial\varphi/\partial\delta$. The transmission coefficient at zero-detuning ($\delta = 0$) is given as

$$T_z = \left|\frac{4G^2 - (2\eta - 1)\kappa\gamma_m}{4G^2 + \kappa\gamma_m}\right|^2, \tag{9}$$

from which we find that the prerequisite for coherent perfect absorption (i.e., $T_z = 0$) is $\eta > 1/2$, viz., external overcoupling $\kappa_{ex} > \kappa_{in}$. For our device, the external coupling coefficient is determined to be $\eta = 0.6$. Figure 5a shows the probe-tone S_{21} transmission response under a set of electromechanical couplings strengths $G/2\pi = [10.46, 15.85, 19.2, 961.07]$ Hz, respectively. Under a weak coupling strength (e.g., $G/2\pi = 10.46$ Hz), the probe-tone transmission spectrum initially shows an additional absorption dip which is more than 30 dB lower than cavity S_{21} background base-line. With coupling rate G increasing, the absorption dip starts to rise until it reaches the background of the microwave cavity S_{21} curve, and finally, a transparency window appears.

The observed electromechanical-induced-absorption (EMIA) and -transparency (EMIT) phenomena can be understood as a result of constructive and destructive interference between two different pathway transitions[99,117–127]. When probe-tone frequency arrives at cavity resonance, a beating (at a mechanical resonance frequency) between pump- and probe-tones coherently excites the mechanical oscillations. Based on the electromechanical coupling, the pump-tone creates a Stokes sideband by absorbing the mechanical excitations. Concurrently, the accompanying anti-Stokes process is substantially suppressed as it is energetically situated below the cutoff frequency of microwave cavity. Additionally, the amplitude of this Stokes sideband depends on the coupling strength, which can be used to control the evolution from EMIA to EMIT.

We now focus on the interference between the photons of the Stokes sideband and probe-tone inside the microwave cavity. When electromechanical coupling rate equals the critical coupling strength $G_c = \sqrt{(2\eta - 1)\kappa\gamma_m/4}$, all created Stokes sideband photons constructively interfere with input probe-tone photons inside the microwave cavity (corresponding to destructive interference outside the cavity), leading to a coherent perfect absorption of transmitted probe-tone (e.g., as shown in the first row of Fig. 5a). Above critical coupling ($G > G_c$), the number of converted Stokes-sideband photons now is more than the number of probe-tone photons. Therefore, only part of the converted Stokes-sideband photons constructively interfered with the probe-tone photons (absorbing them). The remaining Stokes-sideband photons are recorded, and the bottom of the absorption dip starts to rise (e.g., as shown in the second and third row of Fig. 5a, b). While further increasing the electromechanical coupling, the converted Stokes-sideband photons are strong enough to increase the transmission beyond the bare microwave cavity background, as shown in the fourth row of Fig. 5a. As a result, an electromechanically-induced transmission window is observed.

The measured group delays (slow-light time τ) as a function of electromechanical coupling rate are shown in Fig. 5b. With increasing the electromechanical coupling rate G, group delay shows a decreasing trend. We noticed that the rate of group delay decrement changes dramatically when the coupling strength G is in the range where EMIA occurs. However, when G enters the range where EMIT occurs, the rate of group delay decrement remains unchanged. Under the condition of critical coupling $G = G_c$, coherent perfect absorption occurs ($T_z = 0$), and at the same time, a singular point appears in the group delay with infinity slow-light or fast time[117]. Across the critical coupling strength G_c, there is an abrupt transition from infinite group advance to delay. This transition leads to a dramatic change in group delay as the coupling strength G bypasses the singularity. In experimental scenarios, mechanical frequency jitter causes the critical coupling strength condition for achieving infinite group delay to vary, presenting significant challenges. Conversely, the maximum group delay that can be measured in experiments is limited by the frequency stability of the mechanical modes. Here, we report a new record for group delay time, attributed to the inherent advantages in frequency stability. As shown in Fig. 5b, the longest delay time we measured in the experiment is 4035 seconds (more than an hour), achieved through the high Q-factors and extremely low pure dephasing rate of 3C-SiC square membrane. Leveraging exceptional mechanical frequency stability, this interface enables tunable light slowing, achieving group delays of up to an impressive *hour*. This significant improvement over previous pioneering works marks a substantial advancement in optomechanical group delay and slow-light technologies[78,90,98–104]. Figure 5c shows the measured group delay versus probe-tone detuning δ. The maximum delay time occurs at the zero-detuning point and delay time gradually decreases as the coupling rate increases. When the normalized transmission coefficient is close to unity, the energy transfer efficiency reaches its maximum. At the highest transmission efficiency, we emphasize that the delay time can still reach 40.9 ms, which is the longest delay time achieved[99,117–127], to the best of our knowledge.

Sideband cooling of the *dedegeneracy* mechanical modes

The above continuous-fields-based pump-probe experiments mainly demonstrate the performance of our device in storing microwave signals for a long time. For classical applications, the thermal noise in the cavity field or mechanical mode can be neglected. However, for quantum storage, one major obstacle is that the thermal phonons add noise into coherent mechanical excitations during the storage processes. We now show effective optomechanical sideband cooling to prepare mechanical oscillators toward their quantum ground state.

We add two layers of a mechanical damper to isolate external mechanical vibration noises (see Supplementary Note 2), including the pulse tube vibrations. We assume that the phonon occupation of this fundamental mechanical mode can arrive at its equilibration with environment temperature at several hundred millikelvins (mK) provided by the cryostat. Using the Bose-Einstein statistics for mechanical

https://doi.org/10.1038/s41467-025-56497-3

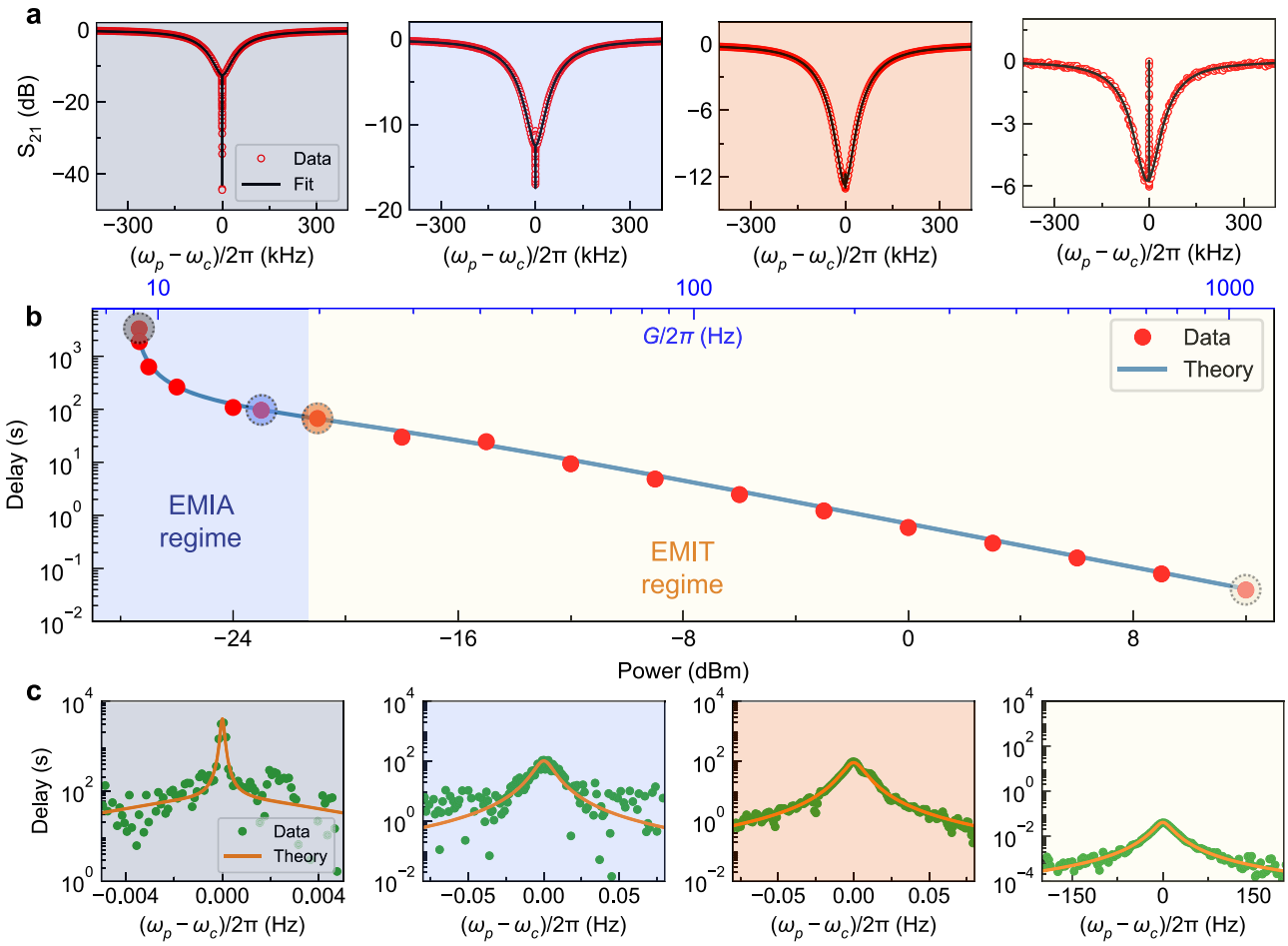

Fig. 5 | Continuous wave pump-probe experiment and ultralong group-delay and slow-light. a The S_{21} transmission spectrum as a function of probe-field frequency detuning $\delta = \omega_p - \omega_c$. Red circles are experimental data, and the black-solid curves are the fitting curves. **b** shows the delay time for a set of driving-tone powers. The red-solid circles represent the experimental data and the blue curve is the theory curve calculated from parameters fitting from **a**. Here, "dBm" is an arbitrary unit and refers to the generator power. The dashed circles are colored according to the minor in **a** and **c**, respectively. The use of blue and beige background colors in **b** signifies EMIA and EMIT regimes, respectively. **c** the delay time as a function of probe-tone frequency detuning δ, wherein green dots and orange curves are experimental data and fitting curves, respectively. **a**, **c** From left to right the pump power is gradually increased, and the corresponding slow-light time is marked by dashed circles, as shown in **b**.

thermal states, i.e., $N_m^{th} = (e^{\hbar\omega_m/k_B T} - 1)^{-1}$, we can extract a calibration constant between the area of mechanical sideband spectrum and the thermal bath phonon occupations in quanta. Here, k_B is the Boltzmann constant constant, and T is the working temperature of the cryostat. We find that the peak area grows linearly with T (see Supplementary Note 7) when the refrigerator's working temperature is above 20 mK, corresponding to an initial phonon occupation of $N_m^{th} = 476$.

To cool the mechanical mode, we continue to use the red-sideband drive with an optimal detuning of $\Delta = -\omega_m$. The scheme can be depicted as that demonstrated in Fig. 1d, but without the probe-tone. In the resolved-sideband regime, the PSD of the output cavity field is finally expressed as the formula given in Eq. (5). Figure 6a shows mechanical ringdown curves under different sideband cooling power P. In the experiment, the ringdown lifetime starts to decrease as cooling power P increases. This can be intuitively understood as the additional optical-damping broadens the linewidth of the mechanical mode, i.e., $\gamma_{tot} = \gamma_{opt} + \gamma_m$. We can obtain the total mechanical damping rate γ_{tot} by fitting the ringdown curves as shown in Fig. 6a. Figure 6b shows that the extracted optical-damping γ_{opt} depends linearly on increasing the sideband cooling power P, which is in good agreement with the theoretical predictions.

Ideally, as the sideband cooling power increases, the number of phonons gradually decreases, and the oscillator enters the ground state. However, in the experiment, the cooling may be limited by microwave heating which raises the bath temperatures of the cavity and of the mechanical resonator. The thermal occupations N_c^{th} and N_m^{th} thus become dependent on the sideband pump power. Noise spectra of cavity emission and typical mechanical sidebands are presented in Supplementary Note 8. Using the function given in Eq. (5) and through the nonlinear least-squares fitting of the PSD, we can obtain the values of N_c^{th} and N_m^{th} under different sideband cooling power or opto-mechanical cooperativity. Using the solutions for $b[\omega]$, the phonon occupation N_m can be derived via equipartition theorem[128,129]. Considering the case of optimal detuning $\Delta = -\omega_m$, and $\kappa^2 \gg (4G^2, \kappa\gamma_m, \gamma_m)$, we find

$$N_m = \frac{\gamma_m}{\gamma_{opt} + \gamma_m} N_m^{th} + \frac{\gamma_{opt}}{\gamma_{opt} + \gamma_m} N_c^{th}. \quad (10)$$

The final steady-state occupations of mechanical mode (N_m), the thermal occupations of cavity field (N_c^{th}) and mechanical mode (N_m^{th}) bathes, as a function of both the cooling power P and optomechanical cooperativity, are summarized in Fig. 6c.

Equation (10) shows that sideband cooling can never reduce the mechanical mode occupancy below the occupancy of the cavity thermal bath. As shown in Fig. 6c, the value of N_m depends mainly on the

https://doi.org/10.1038/s41467-025-56497-3

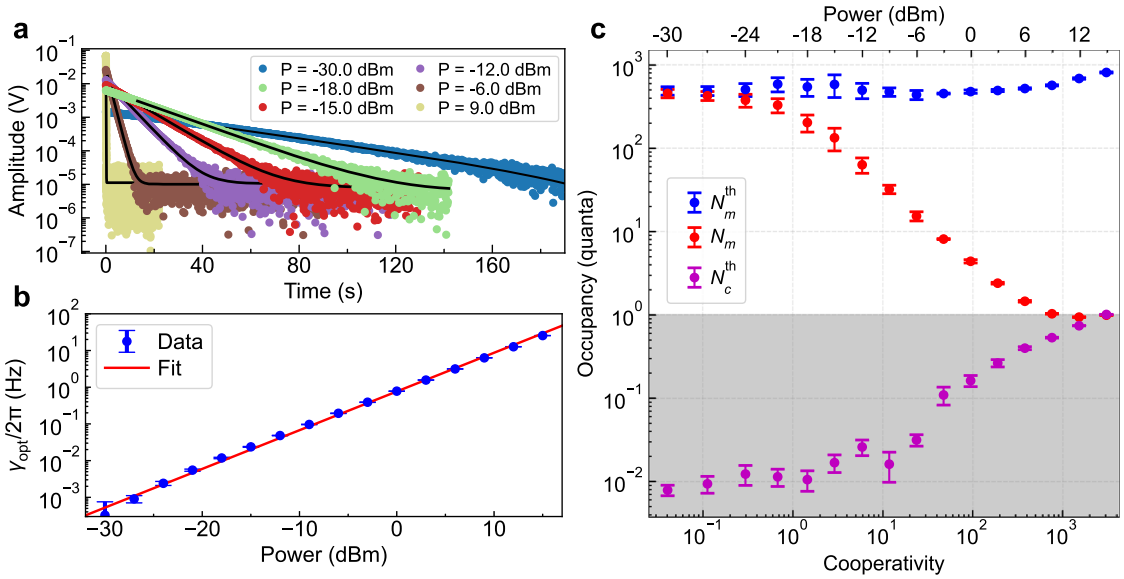

Fig. 6 | Sideband cooling of the mechanical memory mode. a The ringdown measurement of total mechanical linewidth γ_{tot} with a set of sideband cooling powers P. Colored-solid dots are experiment data and black-solid curves represent the fitting. **b** Cavity-field backaction introduces an additional optical-damping γ_{opt} for the mechanical resonator. γ_{opt} exhibits a linear growth with increasing the sideband driving power P. **c** The mechanical occupation is calibrated as the number of motional quanta. N_m^{th} (N_c^{th}) is the effective thermal bath occupation of the mechanical mode (microwave cavity mode), respectively. Error bars equal one standard deviation.

final occupancy number of cavity thermal bath N_c^{th} at the highest powers. In this experiment, the minimum average phonon occupation is $N_m = 0.9 \pm 0.03$. Towards achieving the ground-state cooling, cavity thermal occupancy N_c^{th} must be controlled within one quantum. For currently reported cavity electromechanical systems, such as those based on either crystalline silicon acoustic cavities[77] or amorphous SiN membrane oscillators[22,92,130,131], significant heating effects are observed in the mechanical thermal baths. However, for the 3C-SiC studied in this work, the fundamental drumhead mode of the membrane resonator does not exhibit a significant heating effect, which can be attributed to the extremely high thermal conductivity of SiC in 3C phase.

On-demand state capture, storage, and retrieval

We then investigate the device's performance as an on-demand phononic memory by measuring the capture, storage, and retrieval of itinerant microwave pulses in the time domain. Based on the beam-splitter type optomechanical interaction $H_{BS} = G(a^\dagger b + b^\dagger a)$, the state encoded in an itinerant microwave pulse can be written into and read out of the mechanical memory mode by controlling the pulse sequence of the transfer field. A constant sideband cooling tone is added to initialize the mechanical memory to its ground state. The corresponding optical-damping rate is $\gamma_{opt}^g = 12.6$ Hz. The state capture, storage, and retrieval pulse sequence has been depicted in Fig. 1e. It has been experimentally verified in the literature that matching signal growth rate Γ with sideband cooling rate can result in an optimal state recovery efficiency[22,132]. So, in this stage, we generate a microwave pulse characterized by an amplitude that exhibits exponentially growth at a specified rate of $\Gamma = \gamma_{opt}^g$.

The coherent state arrives at the cavity resonator at the moment of t_1. From t_1 to t_2 (duration 60 ms), when a coherent state arrives inside the microwave cavity, the constant sideband cooling tone begins to play another role, that is transferring the amplitude and phase information of such input signal-pulse into the phononic memory mode of 3C-SiC membrane resonator. As the microwave coherent state is captured, a coherent portion of the mechanical excitations continuously increases. In this stage, the sideband cooling tone is also called as the write field. At the moment of t_2, the writing field is closed, and the captured microwave state is stored as coherent phonons inside our memory device. After a certain period of storage (τ), constant sideband cooling tone is added again (60 ms from t_3 to t_4), which maps the state from phononic mode back to an itinerant microwave pulse. The constant sideband cooling tone retrieves the microwave coherent state and thus is called the readout field in the recovering stage. The pulse sequence is completed after the time of t_4. During the entire process, the itinerant microwave coherent state has experienced the process of capture, storage, and retrieval. In the readout stage, we use an optomechanical phase-insensitive amplification technique (with a blue-detuned sideband pump) to improve the signal-to-noise ratio[133–135].

During the storage procedure, the phononic mode undergoes a re-thermalization process. We now directly present the coherent storage lifetime by recording its thermal decoherence in the time domain. Turning on the readout field, the amplitude and phase of V_{out} encode the state of the mechanical mode after a storage time of τ. The voltage signal V_{out} of recovered itinerant microwave pulses is recorded and analyzed by a spectrum analyzer. The quadrature amplitudes of mechanical motion are obtained by projecting V_{out} onto the local oscillator with frequency ω_{out}:

$$X_1 = C\sum_i V_{out}(t_i)\cos(\omega_{out}t_i),$$
$$X_2 = C\sum_i V_{out}(t_i)\sin(\omega_{out}t_i). \quad (11)$$

The completion of each pulse-sequence measurement generates a single point in the quadrature phase space. We can obtain the state tomography of the retrieved microwave state by repeating the pulse sequence thousands of times. From quadrature distributions, we can distinguish the coherent component of mechanical excitations $N_{coh} = \langle X_1\rangle^2 + \langle X_2\rangle^2$ and incoherent component of thermal occupancy $N_{th}^{\tau} = \langle (X_1 - \langle X_1\rangle)^2\rangle + \langle (X_2 - \langle X_2\rangle)^2\rangle - n_{add}$. Brackets here represent an ensemble average. Given sufficient storage time, we postulate that the mechanical oscillator fully reverts to its initial thermal state, achieving a state of thermal equilibrium with a phonon occupation number of $N_m^{th} = 476$. We thus can calibrate the

https://doi.org/10.1038/s41467-025-56497-3

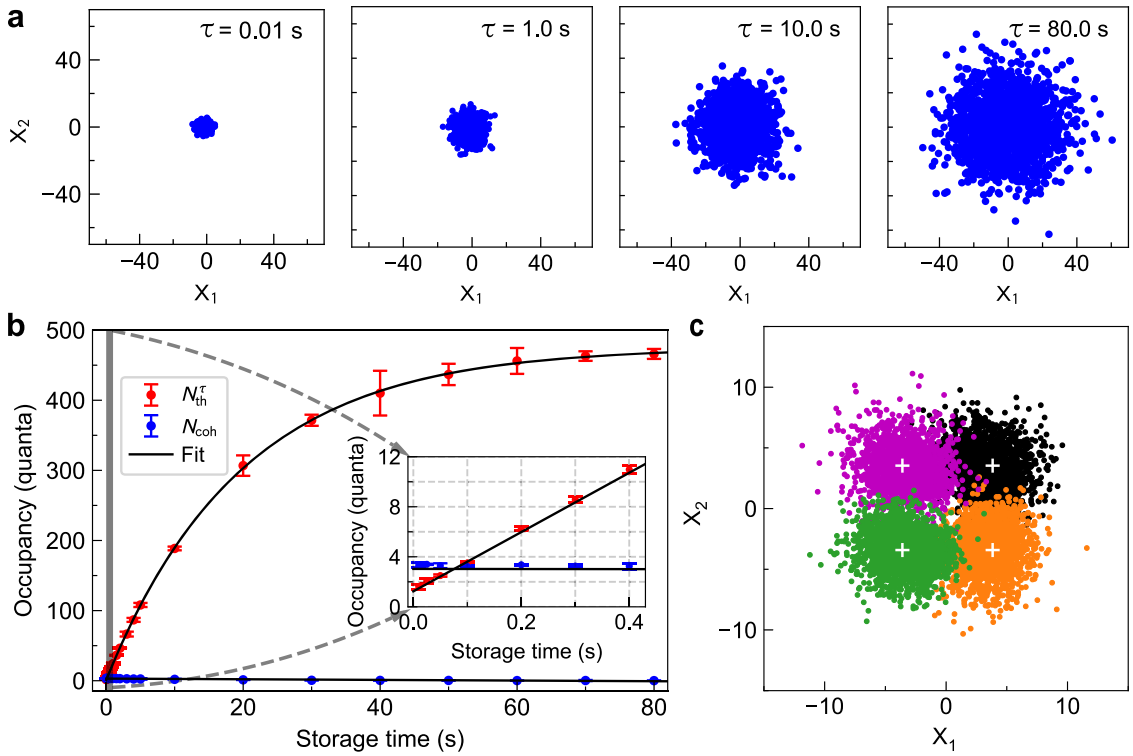

Fig. 7 | On-demand microwave state storage and tomography in the time domain. a Scatter plots of the measured quadratures of motion with coherent input signals for different evolution times $\tau = 0.01, 1, 10, 80$s. One pulse-sequence measurement yields a point (blue dot) in the quadrature phase space. Each figure in **a** is obtained by repeating the pulse-sequence measurements 3000 times. The offset of the center of the scatter plot relative to the origin of the coordinates represents the component of the coherent excitations N_{coh}. **b** The coherent and thermal components of the retrieved microwave pulse after a storage time of τ. The green triangles (red dots) are experimental data of thermal (coherent) occupation N_{th}^{τ} (N_{coh}) with error bars. At the same time, the solid lines are the corresponding exponential fit. **c** The phases of input signal pulses in the protocol of recovered microwave pulse with a phase increment of $\pi/2$.

gain factor C in Eq. (11) and express $X_{1,2}$ in units of quanta. The calibration of the gain factor and the added noise are presented in Supplementary Note 9.

We now demonstrate microwave coherent state storage through the coherent electromechanical interface and the phononic memory mode. The scatter plots of the measured quadratures of the recovered microwave pulses are presented in Fig. 7a, for different storage time $\tau = 0$s, 1s, 10s, 80s, respectively. As the storage interval τ increases, the variance $\sigma^2 = N_{th}^{\tau}$ starts to increase due to the re-thermalization of the phononic memory mode. Figure 7b shows the measured coherent and thermal components of the mechanical memory mode, as a function of the storage time interval τ. The mechanical memory mode takes more than 70 seconds for the free evolution from its ground state to a final thermal equilibrium state. The average photon number of the captured microwave coherent state is 4.2 quanta. The coherent component of phononic mode decays exponentially and the fit of N_{coh} results in $\gamma_m/2\pi = 8.12 \pm 0.19$ mHz, corresponding to an energy decay rate of $T_1 = 19.9 \pm 0.3$ seconds. These experiment data show excellent agreement with the predicted evolution. Coherent storage lifetime is an important figure of merit for characterizing a quantum memory. Zoomed-in area in Fig. 7b shows the thermalization and energy decay of the mechanical memory in shorter evolution intervals. The storage lifetime is determined by the thermal decoherence rate of the mechanical memory, which is calibrated as $\Gamma_{th}/2\pi = 3.85$ Hz, corresponding to a phonon lifetime of $\tau_{coh} = 41.3$ ms. We finally verify the coherence of our electromechanical phononic memory by transferring four microwave coherent states with an $\pi/2$ increment in phase. The state tomography of recovered microwave pulses is presented in Fig. 7c, which shows that the phase of the signal pulse is faithfully recovered after storage.

Coherent energy transfer between distinct high-Q mechanical modes

In the 3C-SiC square membrane-based microwave electromechanical device examined in this study, not only can the (1,3) mode be sideband cooled to its ground state and utilized as a coherent memory, but we can also select other mechanical modes, such as the (3,3) mode. The thermal decoherence rate of the (3,3) mode is $\Gamma_{th}^{3,3}/2\pi = 2.35$ Hz, corresponding to a phonon lifetime of $\tau_{coh} = 67.75$ ms. Coherent manipulation of phonon transport between distinct mechanical modes is essential for preparing mechanical nonclassical states and for potential applications in bosonic coding with long-lived phononic modes. Since these mechanical modes are optomechanically coupled to the same microwave cavity, they can interact through an intermediary microwave field.

By employing a mechanism similar to STIRAP (stimulated Raman adiabatic passage) in atomic physics, we can couple two distinct mechanical resonators using an effective beam-splitter interaction, demonstrating that efficient and coherent state transfer is achievable between these frequency-separated mechanical modes within the same microwave cavity. While energy transfer between two separated mechanical modes has been demonstrated in the classical regime[73,79], in this work, both mechanical modes are initialized in their ground states.

As shown in Fig. 8, we illustrate coherent optomechanical state swapping between two frequency-separated mechanical modes in the quantum regime. The state transfer pulse sequence is similar to the scheme depicted in Fig. 1e, but replaces the storage duration with a swapping pulse operation. By repeating the state-swapping pulse sequence for various durations thousands of times, we can calibrate the coherent and thermal components of the phonon number for each mechanical mode (corresponding to each point in Fig. 8) using the method demonstrated in Fig. 7.

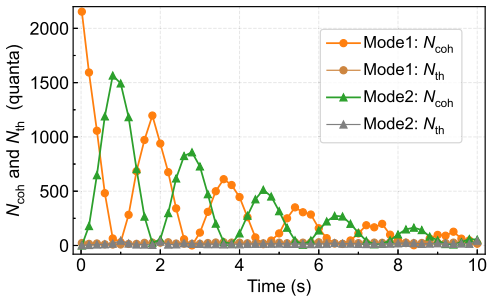

Fig. 8 | Optomechanical state swapping occurs between two mechanical modes, both of which are initially sideband cooled to their ground state. The measurement of the state-swapping pulse sequence, repeated a thousand times, yields scattering points in quadrature phase space that enable us to calibrate the coherent and thermal components of the phonon numbers for each mechanical mode used in the state swapping.

Discussion

We have constructed a microwave cavity electromechanical system comprising a 3D microwave cavity and a 3C-phase SiC membrane resonator. We have confirmed that the low-resistance semiconductor 3C-SiC is compatible with superconducting quantum circuits, ensuring a low electromagnetic loss. The non-uniform tensile stress breaks the membrane's rotational symmetry, leading to the splitting of degenerate superposition modes into near-resonant mode pairs with distinct mode shapes. Both modes in the degeneracy-breaking mode pair exhibit a vertical displacement at the exact center, in stark contrast to the situation where only the constructive superposition mode in the degenerate mode pair has a central vertical displacement, thereby increasing the mechanical modes that the microwave cavity can read. By combining the notch-type asymmetric structure design of the bottom electrode with the breaking of mechanical modes degeneracy, the shared microwave cavity field enables the electromechanical readout of 21 mechanical modes. Additionally, we found that the extremely high thermal conductivity of the 3C-SiC membrane is another advantage for mitigating the notorious mechanical heating effect observed in other optomechanical or electromechanical devices. The 3C-phase SiC membrane chip effectively thermalizes the operating temperature of the refrigerator, resulting in four orders of magnitude improvement in the Q-factors of the mechanical modes compared to the performance measured at room temperature. Nineteen of the detected mechanical modes (over 90%) demonstrate Q-factors exceeding 10^8. Frequency instability and pure dephasing are increasingly prominent limitations for further improving the performance of high Q mechanical resonators. To better highlight the advantages of using a 3C-SiC square membrane as a mechanical resonator in microwave electromechanical devices, the performance of mechanical resonators made from other materials, such as crystalline silicon or amorphous SiN, is summarized in Table 2.

The table illustrates that previously, SiC films were primarily utilized in conjunction with optical microcavities to facilitate cavity optomechanical coupling. Our work introduces the application of crystalline SiC membranes in the realm of microwave electromechanical (EM) coupling. Unlike other single-crystal materials, e.g., crystalline silicon nanobeam[77,93,136], which exhibit extremely low energy decay rate (with a quality factor $Q \sim 10^{10}$), the frequency instability and jitter at low temperatures introduce additional decoherence. This results in a coherence lifetime for the oscillator on the order of hundreds of microseconds ($\tau_{coh} \sim 100\,\mu s$). In contrast, our research demonstrates the exceptional frequency stability of 3C-SiC oscillators at low temperatures, with coherence times approaching the order of a hundred milliseconds, which is over three orders of magnitude greater than that of other single-crystal oscillators. This enhanced frequency stability allows the microwave field group delay induced by 3C-SiC square membrane oscillators to exceed one hour, surpassing the best-reported levels of hundreds of seconds in SiN membrane oscillator systems[22,117].

As a perspective, integrating phonon bandgap engineering and dissipative dilution techniques will further enhance the quality factor of 3C-SiC oscillators. Replacing the 3D aluminum cavity with an annealed copper or on-chip 2D superconducting LC resonator can reduce the cavity field heating effect, enabling a lower phonon occupancy number. Defects in 3C-SiC, such as silicon vacancies (VSi) and carbon vacancies (VC), can serve as qubits with long coherence times. Optical fields can be used to manipulate and detect the quantum states of these single spins. By integrating high-Q and long-lived 3C-SiC mechanical membrane resonators, a functional interface can be established to transfer information between disparate quantum elements, including microwave photons, superconducting qubits, defect spins, and even optical photons. By combining disparate quantum elements through 3C-SiC mechanical resonators, we can enhance functionality and expand the toolbox for quantum information processing[137–139]. Exploring these avenues holds great potential to enable coherent information transfer and advance hybrid quantum architectures with enhanced capabilities.

Methods

Device fabrication

The device consists of a 3D aluminum (Al) superconducting cavity and a mechanical capacitor chip. The Al-rectangle cavity is shaped and polished after machining. The mechanical capacitor chip is assembled by using a flip-chip bonder. The upper parallel-plate electrode is made on a 3C-phase silicon carbide membrane with 400 μm thick silicon frame (Norcada PSCX5050A). The SiC window was metalized with a circular Al electrode deposited by electron beam evaporation (JEB-4, Adnanotek). A commercial ACCμRA flip-chip bonder was used to align the center of the upper layer electrode on the squared SiC window to the center of the bottom parallel-plate electrode of the coupling antenna chip. The main structure of the bottom antenna chip is an H-shaped electrode with 120 nm thick niobium sputtered on a high resistance silicon (orientation of ⟨100⟩) substrate with a thickness of 500 μm. The Nb thin film is sputtered through standard physical vapor deposition technology (Syskey Technology, SP-IC4-A06). The sputter working parameters are 5×10^{-3} hPa, power 150 W, and time 800 s, respectively. To mitigate the influence of oxidation on the resonator performance, the Nb film was placed in nitrogen (a pressure of 1000 Pa) for 35 minutes. The Nb/Si wafer was then subjected to the lithography processes. We selected S1813 photoresist as the coating layer with a spinning rate of 3000 rpm and an operating time of 1 minute. The photoresist was then baked at 115 °C for 2 minutes. We used the DWL 66+ laser lithography tool (Heidelberg Instruments) to transfer the pattern. In the process of laser direct-writing, the laser power, the intensity, the filter, and the focus were set at 70 mW, 30%, 12.5%, and −20%, respectively. The development process was carried out at 1 minute in the MF-319 developer, followed by rinsing in DIW fixing solution. When the pattern was completely transferred, the unwanted Nb film was removed in the RIE process (RIE-10NR, Samco Inc).

Measurement methods

The device was mounted on the 10 mK mixing-chamber plate of a dilution refrigerator and a circulator was used for reflection measurements. The cancellation line is combined with the output line via a directional coupler. By adjusting the amplitude and phase of the canceling tone, the reflected pump tone can be effectively canceled to avoid the HEMT saturation. An arbitrary waveform generator (Tektronix AWG5014C) with a mixer is used to shape the sideband pump-tone (with frequency $\omega_c - \omega_m$), amplify-tone (with frequency

https://doi.org/10.1038/s41467-025-56497-3

Table 2 | The performance of mechanical resonators in optomechanical (OM) and electromechanical (EM) devices

Material	Bandgap isolation	Structure	Frequency	Q factor	Total linewidth	Pure dephasing	Group delay	Ground-state	Coherence time
Al-stairs-drum[98]	no	stairs-circular plate (EM)	$2\pi \cdot 10.69$ MHz	3.6×10^5	$2\pi \cdot 30$ Hz	not report	~5 ms	yes	130 μs
Al-flat-drum[134]	no	flat circular plate (EM)	$2\pi \cdot 1.8$ MHz	1.6×10^7	$2\pi \cdot 0.135$ Hz	$2\pi \cdot 0.09$ Hz	not report	yes	7.7 ms
SiN[99]	no	double clamped beam (EM)	$2\pi \cdot 1.45$ MHz	6×10^5	$2\pi \cdot 14.5$ Hz	not report	3.4 ms	no	not report
SiN[90]	yes	phononic crystal beam (EM)	$2\pi \cdot 4.48$ MHz	5.6×10^5	$2\pi \cdot 8$ Hz	not report	19.9 ms	yes	not report
SiN[92]	yes	Lotus membrane (EM)	$2\pi \cdot 1.48$ MHz	5.7×10^8	$2\pi \cdot 2.6$ mHz	$2\pi \cdot 0.5$ mHz	not report	yes	~100 ms
SiN[22,117]	no	square membrane (EM)	$2\pi \cdot 750$ kHz	7.8×10^7	$2\pi \cdot 9.7$ mHz	not report	~ 500 s	yes	55.7 μs
SiN[78]	yes	Honeycomb lattice (OM)	$2\pi \cdot 2.4$ MHz	10^8	$2\pi \cdot 24$ mHz	not report	23 ms	no	100 μs
crystalline silicon[77]	yes	phononic crystal beam (OM)	$2\pi \cdot 5$ GHz	$\sim4.09\times10^6$	$2\pi \cdot 1.22$ kHz	$2\pi \cdot 1.219$ kHz	not report	yes	130 μs
crystalline silicon[93]	yes	phononic crystal beam (EM)	$2\pi \cdot 5.08$ GHz	$\sim2\times10^5$	$2\pi \cdot 31.8$ kHz	$2\pi \cdot 30$ kHz	not report	yes	5 μs
crystalline silicon[136]	yes	phononic crystal beam (OM)	$2\pi \cdot 5.12$ GHz	$\sim2.58\times10^6$	$2\pi \cdot 1.98$ kHz	$2\pi \cdot 1.42$ kHz	not report	yes	≤112μs
gallium phosphide (GaP)[65]	yes	phononic crystal beam (OM)	$2\pi \cdot 2.81$ GHz	4×10^4	$2\pi \cdot 67$ kHz	$2\pi \cdot 64.5$ kHz	not report	yes	2.37 μs
gallium arsenide (GaAs)[140]	no	phononic crystal beam (OM)	$2\pi \cdot 2.7$ GHz	1.8×10^4	$2\pi \cdot 179$ kHz	not report	not report	yes	0.8 μs
aluminum nitride (AlN)[141]	no	microdisk (OM)	$2\pi \cdot 0.78$ GHz	3.86×10^3	$2\pi \cdot 202$ kHz	not report	0.76 μs	no	not report
lithium niobate ($LiNbO_3$)[142]	yes	phononic crystal beam (OM)	$2\pi \cdot 2.1$ GHz	1.7×10^4	$2\pi \cdot 123$ kHz	not report	not report	no	not report
crystalline diamond[100]	no	microdisk (OM)	$2\pi \cdot 2.14$ GHz	1.12×10^4	$2\pi \cdot 190$ kHz	not report	~5ms	no	not report
3C-SiC[143]	no	microdisk (OM)	$2\pi \cdot 579$ MHz	5.3×10^3	$2\pi \cdot 108$ kHz	not report	not report	no	not report
3C-SiC[144–146]	no	nanowire (OM)	$2\pi \cdot 50$ kHz	10^3	$2\pi \cdot 50$ Hz	not clear	not report	no	not report
4H-SiC[147]	yes	microdisk (OM)	$2\pi \cdot 6.2$ MHz	2.8×10^6	$2\pi \cdot 2.21$ Hz	not report	not report	no	not report
3C-SiC [this work]	no	square membrane (EM)	$2\pi \cdot 871$ kHz mode (1,3)	1.2×10^8	$2\pi \cdot 8.2$ mHz	$2\pi \cdot 0.28$ mHz	4035 s	yes	41.3 ms
3C-SiC [this work]	no	square membrane (EM)	$2\pi \cdot 1.178$ MHz mode (3,3)	2×10^8	$2\pi \cdot 6.04$ mHz	$2\pi \cdot 0.25$ mHz	>5000 s	yes	67.75 ms

The listed Q-factors in the table correspond to the total linewidth rather than solely considering energy decay. For these properties of other oscillators not listed in the table, please refer to the reviews[23,27,148,149]

$\omega_c + \omega_m$), and signal-tone (with frequency ω_c) to pulse. These three tones are combined through a splitter at room temperature and then transmitted down to the device. To increase the on-off switching ratio of the pulses, we used high-speed microwave switchers after the mixer for each tone, respectively. The control signal of the switch and the pulse signal of the mixer are simultaneously generated by the AWG in the marker channel and analog channel. A real-time signal analyzer (Tektronix RSA5126B) is used for digitalizing the output voltage signal. For the state tomography in the time domain, the frequency center of local RSA acquiring is slightly shifted from signal-tone (i.e., fixed at $\omega_c/2\pi$−400 Hz), to make the acquired IQ signal have a small oscillation frequency. The storage time from write-in to readout is controlled by the AWG in the time domain. To synchronize the RSA signal acquisition with a signal pulse, the RSA is triggered by an AWG pulse. For device S_{21} parameter measurement, the PNA (Agilent N5232A) probe tone is also combined into the input line. When taking the S parameter measurement and spectrum measurement, the amplified tone and signal tone are switched off, and the pump tone is always kept on. All instruments are phase-locked by a 10 MHz rubidium frequency standard.

Data availability

All data supporting the findings of this study are available within the article and the Supplementary Information file, or available from the corresponding authors upon request.

References

1. Gerhardt, R. Properties and applications of silicon carbide (BoD–Books on Demand, 2011).
2. Feng, Z. C. Handbook of silicon carbide materials and devices (CRC Press, 2023).
3. Cheung, R. Silicon carbide microelectromechanical systems for harsh environments (World Scientific, 2006).
4. Aharonovich, I. & Toth, M. Silicon carbide goes quantum. *Nat. Phys.* **10**, 93–94 (2014).
5. Boretti, A. Silicon carbide's quantum aspects. *Nat. Photonics* **8**, 88–90 (2014).
6. Castelletto, S. Silicon carbide incorporates quantum gates. *Nat. Mater.* **21**, 8–9 (2022).
7. Lukin, D. M., Guidry, M. A. & Vučković, J. Integrated quantum photonics with silicon carbide: challenges and prospects. *PRX Quantum* **1**, 020102 (2020).
8. Majety, S., Saha, P., Norman, V. A. & Radulaski, M. Quantum information processing with integrated silicon carbide photonics. *J. Appl. Phys.* **131**, 130901 (2022).
9. Awschalom, D. D., Hanson, R., Wrachtrup, J. & Zhou, B. B. Quantum technologies with optically interfaced solid-state spins. *Nat. Photonics* **12**, 516–527 (2018).
10. Elshaari, A. W., Pernice, W., Srinivasan, K., Benson, O. & Zwiller, V. Hybrid integrated quantum photonic circuits. *Nat. Photonics* **14**, 285–298 (2020).
11. Lohrmann, A., Johnson, B. C., McCallum, J. C. & Castelletto, S. A review on single photon sources in silicon carbide. *Rep. Prog. Phys.* **80**, 034502 (2017).
12. Castelletto, S. & Boretti, A. Silicon carbide color centers for quantum applications. *J. Phys. Photonics* **2**, 022001 (2020).
13. Gao, W. B., Imamoglu, A., Bernien, H. & Hanson, R. Coherent manipulation, measurement and entanglement of individual solid-state spins using optical fields. *Nat. Photonics* **9**, 363–373 (2015).
14. Luo, W. et al. Recent progress in quantum photonic chips for quantum communication and internet. *Light Sci. Appl.* **12**, 175 (2023).
15. Luo, Q.-Y. et al. Fabrication and quantum sensing of spin defects in silicon carbide. *Front. Phys.* **11**, 1270602 (2023).
16. Wang, J.-F. et al. Magnetic detection under high pressures using designed silicon vacancy centres in silicon carbide. *Nat. Mater.* **22**, 489–494 (2023).
17. Zhuang, H., Yang, N., Zhang, L., Fuchs, R. & Jiang, X. Electrochemical properties and applications of nanocrystalline, microcrystalline, and epitaxial cubic silicon carbide films. *ACS Appl. Mater. Interfaces* **7**, 10886–10895 (2015).
18. Dao, D. V., Phan, H.-P., Qamar, A. & Dinh, T. Piezoresistive effect of p-type single crystalline 3C-SiC on (111) plane. *RSC Adv.* **6**, 21302–21307 (2016).
19. Phan, H.-P. et al. Single-crystalline 3C-SiC anodically bonded onto glass: an excellent platform for high-temperature electronics and bioapplications. *ACS Appl. Mater. Interfaces* **9**, 27365–27371 (2017).
20. Chatterjee, A. et al. Semiconductor qubits in practice. *Nat. Rev. Phys.* **3**, 157–177 (2021).
21. Yuan, M., Singh, V., Blanter, Y. M. & Steele, G. A. Large cooperativity and microkelvin cooling with a three-dimensional optomechanical cavity. *Nat. Commun.* **6**, 8491 (2015).
22. Liu, Y. et al. Coherent memory for microwave photons based on long-lived mechanical excitations. *npj Quantum Inf.* **9**, 80 (2023).
23. Serra, E. et al. Silicon-nitride nanosensors toward room temperature quantum optomechanics. *J. Appl. Phys.* **130**, 064503 (2021).
24. Høj, D. et al. Ultra-coherent nanomechanical resonators based on inverse design. *Nat. Commun.* **12**, 5766 (2021).
25. Tsaturyan, Y., Barg, A., Polzik, E. S. & Schliesser, A. Ultracoherent nanomechanical resonators via soft clamping and dissipation dilution. *Nat. Nanotechnol.* **12**, 776–783 (2017).
26. Galinskiy, I., Tsaturyan, Y., Parniak, M. & Polzik, E. S. Phonon counting thermometry of an ultracoherent membrane resonator near its motional ground state. *Optica* **7**, 718–725 (2020).
27. Sementilli, L., Romero, E. & Bowen, W. P. Nanomechanical dissipation and strain engineering. *Adv. Funct. Mater.* **32**, 2105247 (2022).
28. Beccari, A. et al. Strained crystalline nanomechanical resonators with quality factors above 10 billion. *Nat. Phys.* **18**, 436–441 (2022).
29. Shin, D. et al. Spiderweb nanomechanical resonators via bayesian optimization: inspired by nature and guided by machine learning. *Adv. Mater.* **34**, 2106248 (2022).
30. Kwon, G. et al. Room-temperature yield and fracture strength of single-crystalline 6H silicon carbide. *J. Mater. Sci.* **50**, 8104–8110 (2015).
31. Phan, H.-P. et al. Ultra-high strain in epitaxial silicon carbide nanostructures utilizing residual stress amplification. *Appl. Phys. Lett.* **110**, 141906 (2017).
32. Anzalone, R., Alberti, A. & La Via, F. Evaluation of 3C-SiC/Si residual stress and curvatures along different wafer direction. *Mater. Lett.* **118**, 130–133 (2014).
33. Rohmfeld, S., Hundhausen, M., Ley, L., Zorman, C. A. & Mehregany, M. Quantitative evaluation of biaxial strain in epitaxial 3C-SiC layers on Si (100) substrates by Raman spectroscopy. *J. Appl. Phys.* **91**, 1113–1117 (2002).
34. Capano, M. A. et al. Residual strains in cubic silicon carbide measured by raman spectroscopy correlated with X-ray diffraction and transmission electron microscopy. *J. Appl. Phys.* **100**, 083514 (2006).
35. Colston, G. et al. Mapping the strain and tilt of a suspended 3C-SiC membrane through micro X-ray diffraction. *Mater. Des.* **103**, 244–248 (2016).
36. Xu, M. et al. High-strength amorphous silicon carbide for nanomechanics. *Adv. Mater.* **10**, 2306513 (2023).
37. Kermany, A. R., Bennett, J. S., Brawley, G. A., Bowen, W. P. & Iacopi, F. Factors affecting the $f \times Q$ product of 3C-SiC microstrings: What is the upper limit for sensitivity? *J. Appl. Phys.* **119**, 055304 (2016).

38. Henry Huang, X. M., Zorman, C. A., Mehregany, M. & Roukes, M. L. Nanodevice motion at microwave frequencies. *Nature* **421**, 496–496 (2003).
39. Kermany, A. R. et al. Microresonators with Q-factors over a million from highly stressed epitaxial silicon carbide on silicon. *Appl. Phys. Lett.* **104**, 081901 (2014).
40. Zorman, C. A. & Parro, R. J. Micro-and nanomechanical structures for silicon carbide MEMS and NEMS. *Phys. Status Solidi* **245**, 1404–1424 (2008).
41. Romero, E. et al. Engineering the dissipation of crystalline micromechanical resonators. *Phys. Rev. Appl.* **13**, 044007 (2020).
42. Anufriev, R., Wu, Y., Ordonez-Miranda, J. & Nomura, M. Nanoscale limit of the thermal conductivity in crystalline silicon carbide membranes, nanowires, and phononic crystals. *NPG Asia Mater.* **14**, 35 (2022).
43. Barnes, A. C., Lee, J., Rawlinson, P. T., Feng, P. X.-L. & Zorman, C. A. Pressure dependence of thin polycrystalline silicon carbide diaphragm resonators. In: *SENSORS, 2012 IEEE*, 1–4 (IEEE, 2012).
44. Zhou, W. et al. Fracture properties of silicon carbide thin films by bulge test of long rectangular membrane. *J. Microelectromechanical Syst.* **17**, 453–461 (2008).
45. Nguyen, T.-K. et al. Superior robust ultrathin single-crystalline silicon carbide membrane as a versatile platform for biological applications. *ACS Appl. Mater. Interfaces* **9**, 41641–41647 (2017).
46. Ockeloen-Korppi, C. et al. Stabilized entanglement of massive mechanical oscillators. *Nature* **556**, 478–482 (2018).
47. Riedinger, R. et al. Remote quantum entanglement between two micromechanical oscillators. *Nature* **556**, 473–477 (2018).
48. Suh, J. et al. Mechanically detecting and avoiding the quantum fluctuations of a microwave field. *Science* **344**, 1262–1265 (2014).
49. Mercier de Lépinay, L., Ockeloen-Korppi, C. F., Woolley, M. J. & Sillanpää, M. A. Quantum mechanics–free subsystem with mechanical oscillators. *Science* **372**, 625–629 (2021).
50. Kurizki, G. et al. Quantum technologies with hybrid systems. *Proc. Natl Acad. Sci.* **112**, 3866–3873 (2015).
51. Han, X., Fu, W., Zou, C.-L., Jiang, L. & Tang, H. X. Microwave-optical quantum frequency conversion. *Optica* **8**, 1050–1064 (2021).
52. Clerk, A. A., Lehnert, K. W., Bertet, P., Petta, J. R. & Nakamura, Y. Hybrid quantum systems with circuit quantum electrodynamics. *Nat. Phys.* **16**, 257–267 (2020).
53. Vivoli, V. C., Barnea, T., Galland, C. & Sangouard, N. Proposal for an optomechanical bell test. *Phys. Rev. Lett.* **116**, 070405 (2016).
54. Hofer, S. G., Lehnert, K. W. & Hammerer, K. Proposal to test bell's inequality in electromechanics. *Phys. Rev. Lett.* **116**, 070406 (2016).
55. Marinković, I. et al. Optomechanical bell test. *Phys. Rev. Lett.* **121**, 220404 (2018).
56. Fiaschi, N. et al. Optomechanical quantum teleportation. *Nat. Photonics* **15**, 817–821 (2021).
57. Belenchia, A. et al. Tests of quantum-gravity-induced nonlocality via optomechanical experiments. *Phys. Rev. D.* **95**, 026012 (2017).
58. Gely, M. F. & Steele, G. A. Superconducting electro-mechanics to test diósi–penrose effects of general relativity in massive superpositions. *AVS Quantum Sci.* **3**, 035601 (2021).
59. Liu, Y., Mummery, J., Zhou, J. & Sillanpää, M. A. Gravitational forces between nonclassical mechanical oscillators. *Phys. Rev. Appl.* **15**, 034004 (2021).
60. Cleland, A. Y., Wollack, E. A. & Safavi-Naeini, A. H. Studying phonon coherence with a quantum sensor. *Nat. Commun.* **15**, 4979 (2024).
61. Sahu, R. et al. Quantum-enabled operation of a microwave-optical interface. *Nat. Commun.* **13**, 1276 (2022).
62. Arnold, G. et al. Converting microwave and telecom photons with a silicon photonic nanomechanical interface. *Nat. Commun.* **11**, 4460 (2020).
63. Weaver, M. J. et al. An integrated microwave-to-optics interface for scalable quantum computing. *Nat. Nanotechnol.* **19**, 166–172 (2024).
64. Hönl, S. et al. Microwave-to-optical conversion with a gallium phosphide photonic crystal cavity. *Nat. Commun.* **13**, 2065 (2022).
65. Stockill, R. et al. Ultra-low-noise microwave to optics conversion in gallium phosphide. *Nat. Commun.* **13**, 6583 (2022).
66. Shen, M. et al. Photonic link from single-flux-quantum circuits to room temperature. *Nat. Photonics* **18**, 371–378 (2024).
67. Delaney, R. et al. Superconducting-qubit readout via low-backaction electro-optic transduction. *Nature* **606**, 489–493 (2022).
68. Mirhosseini, M., Sipahigil, A., Kalaee, M. & Painter, O. Superconducting qubit to optical photon transduction. *Nature* **588**, 599–603 (2020).
69. Kleckner, D. et al. Optomechanical trampoline resonators. *Opt. Express* **19**, 19708–19716 (2011).
70. Barzanjeh, S. et al. Stationary entangled radiation from micromechanical motion. *Nature* **570**, 480–483 (2019).
71. Manjeshwar, S. K. et al. High-Q trampoline resonators from strained crystalline ingap for integrated free-space optomechanics. *Nano Lett.* **23**, 5076–5082 (2023).
72. Weaver, M. J. et al. Nested trampoline resonators for optomechanics. *Appl. Phys. Lett.* **108**, 033501 (2016).
73. Weaver, M. J. et al. Coherent optomechanical state transfer between disparate mechanical resonators. *Nat. Commun.* **8**, 824 (2017).
74. Bereyhi, M. J. et al. Hierarchical tensile structures with ultralow mechanical dissipation. *Nat. Commun.* **13**, 3097 (2022).
75. Fedorov, S. A., Beccari, A., Engelsen, N. J. & Kippenberg, T. J. Fractal-like mechanical resonators with a soft-clamped fundamental mode. *Phys. Rev. Lett.* **124**, 025502 (2020).
76. Brubaker, B. M. et al. Optomechanical ground-state cooling in a continuous and efficient electro-optic transducer. *Phys. Rev. X* **12**, 021062 (2022).
77. MacCabe, G. S. et al. Nano-acoustic resonator with ultralong phonon lifetime. *Science* **370**, 840–843 (2020).
78. Kristensen, M. B., Kralj, N., Langman, E. C. & Schliesser, A. Long-lived and efficient optomechanical memory for light. *Phys. Rev. Lett.* **132**, 100802 (2024).
79. Fedoseev, V., Luna, F., Hedgepeth, I., Löffler, W. & Bouwmeester, D. Stimulated raman adiabatic passage in optomechanics. *Phys. Rev. Lett.* **126**, 113601 (2021).
80. Planz, E., Xi, X., Capelle, T., Langman, E. C. & Schliesser, A. Membrane-in-the-middle optomechanics with a soft-clamped membrane at millikelvin temperatures. *Opt. Express* **31**, 41773–41782 (2023).
81. Huang, G., Beccari, A., Engelsen, N. J. & Kippenberg, T. J. Room-temperature quantum optomechanics using an ultralow noise cavity. *Nature* **626**, 512–516 (2024).
82. Saarinen, S. A., Kralj, N., Langman, E. C., Tsaturyan, Y. & Schliesser, A. Laser cooling a membrane-in-the-middle system close to the quantum ground state from room temperature. *Optica* **10**, 364–372 (2023).
83. Norte, R. A., Moura, J. P. & Gröblacher, S. Mechanical resonators for quantum optomechanics experiments at room temperature. *Phys. Rev. Lett.* **116**, 147202 (2016).
84. Reinhardt, C., Müller, T., Bourassa, A. & Sankey, J. C. Ultralow-noise SiN trampoline resonators for sensing and optomechanics. *Phys. Rev. X* **6**, 021001 (2016).

85. Ghadimi, A. H. et al. Elastic strain engineering for ultralow mechanical dissipation. *Science* **360**, 764–768 (2018).
86. Bereyhi, M. J. et al. Perimeter modes of nanomechanical resonators exhibit quality factors exceeding 10^9 at room temperature. *Phys. Rev. X* **12**, 021036 (2022).
87. Reetz, C. et al. Analysis of membrane phononic crystals with wide band gaps and low-mass defects. *Phys. Rev. Appl.* **12**, 044027 (2019).
88. Shaniv, R., Keshava, S. K., Reetz, C. & Regal, C. A. Understanding the quality factor of mass-loaded tensioned resonators. *Phys. Rev. Appl.* **19**, L031006 (2023).
89. Kalaee, M. et al. Quantum electromechanics of a hypersonic crystal. *Nat. Nanotechnol.* **14**, 334–339 (2019).
90. Fink, J. M. et al. Quantum electromechanics on silicon nitride nanomembranes. *Nat. Commun.* **7**, 12396 (2016).
91. Barzanjeh, S. et al. Mechanical on-chip microwave circulator. *Nat. Commun.* **8**, 953 (2017).
92. Seis, Y. et al. Ground state cooling of an ultracoherent electromechanical system. *Nat. Commun.* **13**, 1507 (2022).
93. Bozkurt, A. et al. A quantum electromechanical interface for long-lived phonons. *Nat. Phys.* **19**, 1326–1332 (2023).
94. Meng, F., Ma, J., He, J. & Li, W. Phonon-limited carrier mobility and temperature-dependent scattering mechanism of 3C-SiC from first principles. *Phys. Rev. B* **99**, 045201 (2019).
95. Cheng, Z. et al. High thermal conductivity in wafer-scale cubic silicon carbide crystals. *Nat. Commun.* **13**, 7201 (2022).
96. Yan, X. et al. Single-defect phonons imaged by electron microscopy. *Nature* **589**, 65–69 (2021).
97. Maillet, O., Subero, D., Peltonen, J. T., Golubev, D. S. & Pekola, J. P. Electric field control of radiative heat transfer in a superconducting circuit. *Nat. Commun.* **11**, 4326 (2020).
98. Teufel, J. D. et al. Circuit cavity electromechanics in the strong-coupling regime. *Nature* **471**, 204–208 (2011).
99. Zhou, X. et al. Slowing, advancing and switching of microwave signals using circuit nanoelectromechanics. *Nat. Phys.* **9**, 179–184 (2013).
100. Lake, D. P., Mitchell, M., Sukachev, D. D. & Barclay, P. E. Processing light with an optically tunable mechanical memory. *Nat. Commun.* **12**, 663 (2021).
101. Shandilya, P. K., Lake, D. P., Mitchell, M. J., Sukachev, D. D. & Barclay, P. E. Optomechanical interface between telecom photons and spin quantum memory. *Nat. Phys.* **17**, 1420–1425 (2021).
102. Merklein, M., Stiller, B., Vu, K., Madden, S. J. & Eggleton, B. J. A chip-integrated coherent photonic-phononic memory. *Nat. Commun.* **8**, 574 (2017).
103. Lu, T.-X., Xiao, X., Chen, L.-S., Zhang, Q. & Jing, H. Magnon-squeezing-enhanced slow light and second-order sideband in cavity magnomechanics. *Phys. Rev. A* **107**, 063714 (2023).
104. Wang, B., Liu, Z.-X., Kong, C., Xiong, H. & Wu, Y. Mechanical exceptional-point-induced transparency and slow light. *Opt. Express* **27**, 8069–8080 (2019).
105. Aspelmeyer, M., Kippenberg, T. J. & Marquardt, F. Cavity optomechanics. *Rev. Mod. Phys.* **86**, 1391 (2014).
106. Clerk, A. A., Devoret, M. H., Girvin, S. M., Marquardt, F. & Schoelkopf, R. J. Introduction to quantum noise, measurement, and amplification. *Rev. Mod. Phys.* **82**, 1155–1208 (2010).
107. Hertzberg, J. B. et al. Back-action-evading measurements of nanomechanical motion. *Nat. Phys.* **6**, 213–217 (2010).
108. Yuan, M., Cohen, M. A. & Steele, G. A. Silicon nitride membrane resonators at millikelvin temperatures with quality factors exceeding 10^8. *Appl. Phys. Lett.* **107**, 263501 (2015).
109. Guria, C. et al. Resolving the topology of encircling multiple exceptional points. *Nat. Commun.* **15**, 1369 (2024).
110. Peterson, R. W. et al. Laser cooling of a micromechanical membrane to the quantum backaction limit. *Phys. Rev. Lett.* **116**, 063601 (2016).
111. Piergentili, P., Li, W., Natali, R., Vitali, D. & Di Giuseppe, G. Absolute determination of the single-photon optomechanical coupling rate via a hopf bifurcation. *Phys. Rev. Appl.* **15**, 034012 (2021).
112. Yang, C., Wei, X., Sheng, J. & Wu, H. Phonon heat transport in cavity-mediated optomechanical nanoresonators. *Nat. Commun.* **11**, 4656 (2020).
113. Yang, F. et al. Spatial modulation of nonlinear flexural vibrations of membrane resonators. *Phys. Rev. Lett.* **122**, 154301 (2019).
114. Zhou, X. et al. High-Q silicon nitride drum resonators strongly coupled to gates. *Nano Lett.* **21**, 5738–5744 (2021).
115. Yang, F. et al. Persistent response in an ultrastrongly driven mechanical membrane resonator. *Phys. Rev. Lett.* **127**, 014304 (2021).
116. Wu, S. et al. Hybridized frequency combs in multimode cavity electromechanical system. *Phys. Rev. Lett.* **128**, 153901 (2022).
117. Liu, Y. et al. Optomechanical anti-lasing with infinite group delay at a phase singularity. *Phys. Rev. Lett.* **127**, 273603 (2021).
118. Agarwal, G. S. & Huang, S. Electromagnetically induced transparency in mechanical effects of light. *Phys. Rev. A* **81**, 041803(R) (2010).
119. Weis, S. et al. Optomechanically induced transparency. *Science* **330**, 1520–1523 (2010).
120. Safavi-Naeini, A. H. et al. Electromagnetically induced transparency and slow light with optomechanics. *Nature* **472**, 69–73 (2011).
121. Karuza, M. et al. Optomechanically induced transparency in a membrane-in-the-middle setup at room temperature. *Phys. Rev. A* **88**, 013804 (2013).
122. Dong, C.-H. et al. Brillouin-scattering-induced transparency and non-reciprocal light storage. *Nat. Commun.* **6**, 6193 (2015).
123. Kim, J., Kuzyk, M. C., Han, K., Wang, H. & Bahl, G. Non-reciprocal Brillouin scattering induced transparency. *Nat. Phys.* **11**, 275–280 (2015).
124. Fan, L., Fong, K. Y., Poot, M. & Tang, H. X. Cascaded optical transparency in multimode-cavity optomechanical systems. *Nat. Commun.* **6**, 5850 (2015).
125. Hocke, F. et al. Electromechanically induced absorption in a circuit nano-electromechanical system. *N. J. Phys.* **14**, 123037 (2012).
126. Xiong, H. & Wu, Y. Fundamentals and applications of optomechanically induced transparency. *Appl. Phys. Rev.* **5**, 031305 (2018).
127. Liu, Y.-C., Li, B.-B. & Xiao, Y.-F. Electromagnetically induced transparency in optical microcavities. *Nanophotonics* **6**, 789–811 (2017).
128. Dobrindt, J. M., Wilson-Rae, I. & Kippenberg, T. J. Parametric normal-mode splitting in cavity optomechanics. *Phys. Rev. Lett.* **101**, 263602 (2008).
129. Rocheleau, T. et al. Preparation and detection of a mechanical resonator near the ground state of motion. *Nature* **463**, 72–75 (2010).
130. Liu, Y., Zhou, J., Mercier de Lépinay, L. & Sillanpää, M. A. Quantum backaction evading measurements of a silicon nitride membrane resonator. *N. J. Phys.* **24**, 083043 (2022).
131. Higginbotham, A. P. et al. Harnessing electro-optic correlations in an efficient mechanical converter. *Nat. Phys.* **14**, 1038–1042 (2018).
132. Palomaki, T. A., Harlow, J. W., Teufel, J. D., Simmonds, R. W. & Lehnert, K. W. Coherent state transfer between itinerant microwave fields and a mechanical oscillator. *Nature* **495**, 210–214 (2013).
133. Massel, F. et al. Multimode circuit optomechanics near the quantum limit. *Nat. Commun.* **3**, 987 (2012).

134. Youssefi, A., Kono, S., Chegnizadeh, M. & Kippenberg, T. J. A squeezed mechanical oscillator with millisecond quantum decoherence. *Nat. Phys.* **19**, 1697–1702 (2023).
135. Reed, A. P. et al. Faithful conversion of propagating quantum information to mechanical motion. *Nat. Phys.* **13**, 1163–1167 (2017).
136. Wallucks, A., Marinković, I., Hensen, B., Stockill, R. & Gröblacher, S. A quantum memory at telecom wavelengths. *Nat. Phys.* **16**, 772–777 (2020).
137. Barzanjeh, S. et al. Optomechanics for quantum technologies. *Nat. Phys.* **18**, 15–24 (2022).
138. Chu, Y. & Gröblacher, S. A perspective on hybrid quantum opto- and electromechanical systems. *Appl. Phys. Lett.* **117**, 150503 (2020).
139. Xu, X.-B., Wang, W.-T., Sun, L.-Y. & Zou, C.-L. Hybrid superconducting photonic-phononic chip for quantum information processing. *Chip* **1**, 100016 (2022).
140. Forsch, M. et al. Microwave-to-optics conversion using a mechanical oscillator in its quantum ground state. *Nat. Phys.* **16**, 69–74 (2020).
141. Fong, K. Y., Fan, L., Jiang, L., Han, X. & Tang, H. X. Microwave-assisted coherent and nonlinear control in cavity piezo-optomechanical systems. *Phys. Rev. A* **90**, 051801 (2014).
142. Jiang, W. et al. Lithium niobate piezo-optomechanical crystals. *Optica* **6**, 845–853 (2019).
143. Lu, X., Lee, J. Y. & Lin, Q. High-frequency and high-quality silicon carbide optomechanical microresonators. *Sci. Rep.* **5**, 17005 (2015).
144. Reigue, A. et al. Cavity nano-optomechanics with suspended subwavelength-sized nanowires. *Phys. Rev. Appl.* **20**, 014025 (2023).
145. Fogliano, F. et al. Mapping the cavity optomechanical interaction with subwavelength-sized ultrasensitive nanomechanical force sensors. *Phys. Rev. X* **11**, 021009 (2021).
146. Mercier de Lépinay, L. et al. A universal and ultrasensitive vectorial nanomechanical sensor for imaging 2D force field. *Nat. Nanotechnol.* **12**, 156–162 (2017).
147. Hamelin, B., Yang, J., Daruwalla, A., Wen, H. & Ayazi, F. Monocrystalline silicon carbide disk resonators on phononic crystals with ultra-low dissipation bulk acoustic wave modes. *Sci. Rep.* **9**, 18698 (2019).
148. Schmid, S., Villanueva, L. G. & Roukes, M. L. Fundamentals of nanomechanical resonators, vol. 49 (Springer, 2016).
149. Engelsen, N. J., Beccari, A. & Kippenberg, T. J. Ultrahigh-quality-factor micro-and nanomechanical resonators using dissipation dilution. *Nat. Nanotechnol.* **19**, 725–737 (2024).

Acknowledgements

This work is supported by the National Natural Science Foundation of China (Grants No. 92365210). Y.L. acknowledges the support of the Beijing Municipal Science and Technology Commission (Grant No. Z221100002722011), Beijing Natural Science Foundation (Z240007), and the Young Elite Scientists Sponsorship Program by CAST (Grant No. 2023QNRC001). This work is also supported by the National Key Research and Development Program of China (Grant No. 2022YFA1405200) and the National Natural Science Foundation of China (No. 12374325, No. 62074091, No. 12304387). We acknowledge the facilities and technical support of Otaniemi research infrastructure for Micro and Nanotechnologies (OtaNano). The work was supported by the European Research Council (101019712). The work was performed as part of the Research Council of Finland Centre of Excellence program (project 336810). We acknowledge funding from the European Union's Horizon 2020 research and innovation program under the QuantERA II Programme (13352189).

Author contributions

Y.L. carried out the device design, fabrication, and drafted the manuscript. H.W. metalizes the SiC membrane. H.S. conducts the room temperature Doppler measurements. Q.L., Y.L., and T.L. developed the measurement schemes. Y.L. and M.A.S. conceived the project and coordinated the research. All authors analyzed the measurement results and gave their final approval for publication.

Competing interests

The authors declare no competing interests.

Additional information

Supplementary information The online version contains supplementary material available at https://doi.org/10.1038/s41467-025-56497-3.

Correspondence and requests for materials should be addressed to Yulong Liu or Tiefu Li.

Peer review information *Nature Communications* thanks the anonymous reviewers for their contribution to the peer review of this work. A peer review file is available.